ISSN 0915-633X

NATIONAL INSTITUTE FOR FUSION SCIENCE

Design Study of a Plasma-Loaded CRM Using TPD-II Machine

K. Minami

(Received - June 11, 2007)

NIFS-880 Aug. 2007

RESEARCH REPORT
NIFS Series

TOKI, JAPAN

Design Study of a Plasma-Loaded CRM Using TPD-II Machine

Kazuo MINAMI

Faculty of Engineering, Tokyo Denki University, Chiyoda-Ku, Tokyo 101-8457, Japan
kminami@msa.biglobe.ne.jp

Abstract

Design study of an experiment for plasma-loaded cyclotron resonance maser (CRM) utilizing TPD-II Machine at NIFS, Japan is described in some detail. The principle of gyrotrons has been believed the CRM instability. However, all the existing linear theories of CRM instability include unphysical modes unstable at infinite values of axial wavenumber that can never be observed experimentally. To overcome the difficulty, we derive and analyze numerically an exact linear dispersion relation of a large orbit electron beam for CRM, and removed the unphysical modes. However, the relation is found to include two principles of cyclotron emission with oscillation frequencies above and below the branch of fast electron cyclotron wave. The former is CRM instability, and the latter is named Cherenkov instability in the azimuthal direction (CIAD). It is noted that the CIAD we found remains only a proposal of a new mechanism for cyclotron emission until the physical existence is verified experimentally. To verify the CIAD, the design study of a plasma-loaded CRM has been carried out. The apparatus consists of two portions installed in the TPD-II: A pair of helical wiggler windings to create a mono-energetic beam with 15 keV and pitch factor $V_\theta / V_z \geq 1$, and microwave circuits including a cylindrical TE_{011} mode cavity with resonant frequency 3.45 GHz. For high plasma density $n \geq 1.5 \times 10^{11}$ cm^{-3} from TPD-II, the CRM instability may be suppressed and the CIAD will take turn. The present experimental study contributes to a deeper understanding and a widened future prospect in gyrotron physics.

Keywords: Cavity, Cherenkov instability in azimuthal direction, CRM instability, cyclotron resonance maser, fast wave, gyrotron, negative absorption, microwave, slow wave, TPD-II, wiggler.

List of Contents

Flow Chart of This Research Report

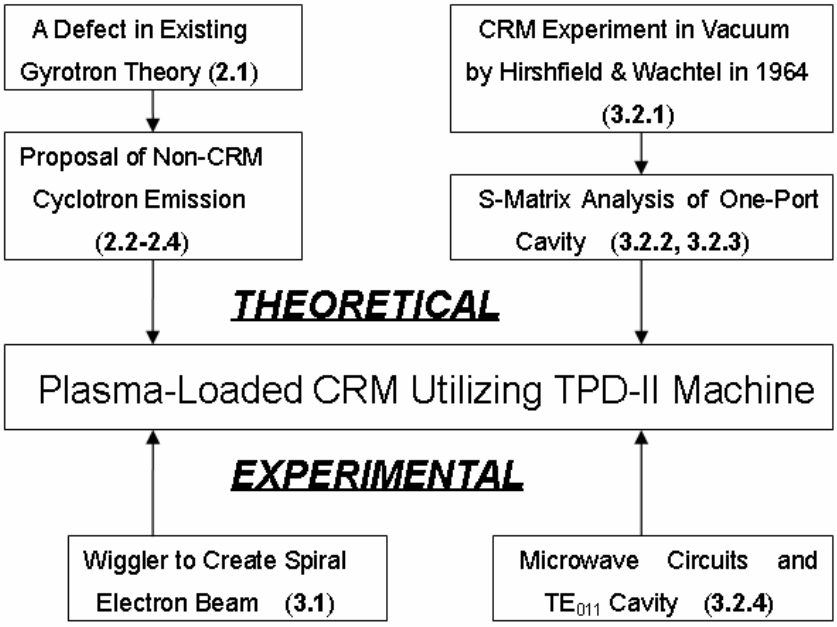

List of Notations

Notation	Definition ([1] means a dimensionless quantity)
a	Radius of helical windings of wiggler [m] in **3.1**
B_0	Axial magnetic field at cavity [T] in **2** and **3.1** Half half-width of resonant curve of cavity [s^{-1}] in **3.2.2**
B_s	Axial magnetic field at the wiggler [T] in **3.1**
b_t	Right-hand circularly polarized dc magnetic field produced by wiggler [Gauss] in **3.1**
c	Light velocity in vacuum 3×10^8 [m/s]
E_b	Beam energy [keV]
f_c	Electron cyclotron frequency [Hz]
h	Coupling constant proportional to hole size of one-port cavity [1] in **3.2**
I_b	Beam current [A]
I_{tot}	DC current flowing the windings of wiggler [A] in **3.1**
k_z	Axial wavenumber [m^{-1}]
L	Total length of wiggler windings in **3.1** [m]
l	Mode number in the azimuthal direction in **2**, Axial length of cavity [m] in **3.2**
N	Number of gyrations in cavity [1]
n	Beam density [m^{-3}]
p	Phenomenological factor [1] in **3.2.3**, negative absorption arises for $\mid p \mid > 1$
Q_e	External Q value of a cavity [1] in **3.2.2**
Q_u	Unloaded Q value of the cavity [1] in **3.2.2**

Q_0	Loaded Q value of the cavity [1] in **3.2.2**
r_b	Radius of thin annular beam [m] in **2**
r_{cav}	Radius of cylindrical waveguide [m] in **2**
R	Reflection coefficient from the cavity [1] in **3.2.2**
$R_{\max}$	Reflection coefficient from the cavity at the resonance [1] in **3.2**
s	Coupling factor between cavity and external circuit given by Q_u / Q_e [1] in **3.2.2**
T	Transmission coefficient through the cavity [1] in **3.2.4**
U	Phenomenological potential well in the radial direction [V] in Appendix A
V_θ	Azimuthal velocity of the spiraling beam [m/s]
V_z	Axial velocity of the spiraling beam [m/s]
α	Pitch factor V_θ / V_z [1] in **2** and **3.1,** Round-trip attenuation of microwave in cavity [m^{-1}] in **3.2.2**
β	$\lvert V \rvert / c$ [1] or wavenumber in waveguide [m^{-1}]
γ	Relativistic factor [1]
γ_0	Initial relativistic factor [1]
ε	Thickness of infinitely thin annular beam [m] , $\varepsilon \to 0$
$\boldsymbol{\kappa}$	Surface current density [A/m] in **2**
λ_c	Cutoff wavelength in cavity [m] in **3.2.2**
λ_0 '	Free space wavelength in vacuum [m] in **3.2.2**
λ_w	Periodic length of helical windings of wiggler [m] in **3.1**
θ	Coordinate in the azimuthal direction [1] in **2.2 -2.4**, Phase of microwave in cavity [1] in **3.2.2**
τ	Time normalized by gyration time [1] in **2.4,** Time constant of cavity [s] in **3.2.2**
ω	Oscillation angular frequency [s^{-1}]
ω_0	Resonant angular frequency of cavity [s^{-1}] in **3.2.2**
$\tilde{\Omega}$	Initial electron cyclotron frequency $eB_0 / m\gamma_0$ [s^{-1}]
Ω	Electron cyclotron frequency $eB_0 / m\gamma$ [s^{-1}] in **2.4**
Δ	Small but finite thickness of annular beam [m] in **2.3**, $\Delta \neq 0$

1. Introduction

1.1 How defective is the conventional theory of CRM instability?

The principle of gyrotrons, high-power millimeter microwave sources indispensable for fusion research, is believed cyclotron resonance maser (CRM) instability [1-3]. The CRM was verified in an experiment in which negative absorption was observed for $\omega > \tilde{\Omega}$ [4]. Here, ω and $\tilde{\Omega} = eB_0/\gamma_0 m$ are, respectively, oscillation angular frequency and relativistic electron cyclotron frequency.

However, all the existing linear dispersion relations of CRM instability [5-8] include unphysical modes unstable at infinite values of axial wavenumber k_z in slow wave region, $\omega/k_z < c$, that can never be observed experimentally. Here, c is the velocity of light in vacuum. These unphysical modes will be discussed in the subsequent section. It should be emphasized that the results from the linear CRM theory reported up to date are quantitatively erroneous because of the presence of the unphysical modes, no matter how people have trusted. No dispersion relation of CRM instability, in which the finite Larmor radius effect of gyrating relativistic electrons at the beam-vacuum interface is correctly analyzed, has been reported.

1.2 Why is it necessary to study the new principle of cyclotron emission?

To overcome the difficulty, we derive and analyze numerically an exact linear dispersion relation of CRM for a large orbit (LO, hereafter) electron beam, for the first time in the history of the CRM research [9, 10]. The conventional unphysical modes are replaced by stable modes near the fast cyclotron mode. Here, LO means that all the electrons have an identical location of guiding center on the center axis of waveguide.

It is found, however, that our dispersion relation includes two principles of cyclotron emission with oscillation frequencies above and below the branch of relativistic fast electron cyclotron wave $\omega = \tilde{\Omega} + V_z k_z$. The former is well-known CRM instability $(\omega > \tilde{\Omega} + V_z k_z)$, and the latter $(\omega < \tilde{\Omega} + V_z k_z)$ is named **Cherenkov instability in the azimuthal direction (CIAD)**. The reason why the CIAD has not been included in the existing dispersion relations is that the boundary conditions with inevitable finite Larmor radius effect at beam-vacuum interface were not analyzed correctly. The CIAD arises logically whenever distinct high density beam-vacuum interface is present. In order to understand the dispersion relations of the CRM instability more correctly, one must take into account the logical presence of the CIAD.

The new principle of cyclotron emission of CIAD is resulted from a constrained gyration model assuming the interruption by neutralizing ions in high-density beams [9]. The physical reason for the model is described in Appendix A. The CIAD is expected to arise at an oscillation frequency $\omega < \tilde{\Omega} + V_z k_z$ in fast wave device region, namely, $\omega/k_z > c$. Our novel and strange model of the constrained electron gyration has not been known up to date in the gyrotron community over the world. However, it really has an exact solution for cyclotron instabilities including CRM by taking into account the finite Larmor radius effect of gyrating electrons at the beam-vacuum interface correctly for the first time in CRM analyses. The CIAD might have happened in previous CRM experiments with high density intense relativistic electron beams (IREBs) produced by cold cathodes [11].

It is also shown [10] that, for tenuous electron beams such as $\omega_b^2 \ll \tilde{\Omega}^2$, the CRM instability $\omega > \tilde{\Omega} + V_z k_z$ caused by free gyration model is the principle of cyclotron radiation. On the other hand, in high density neutralized electron beams such as $\omega_b^2 \gg \tilde{\Omega}^2$, the CIAD $\omega < \tilde{\Omega} + V_z k_z$ obtained by the constrained gyration model will lead to the excitation of microwaves. The latter instability survives even for non-relativistic electron beams, and disappears in ultra-relativistic beams. Both instabilities might co-exist at the same time in non-uniform or incompletely neutralized beams. The CIAD may be an alternative or possibly a co-existing mechanism of cyclotron emission

in microwave devices including the gyrotrons, when high density neutralized beams are working.

1.3 Significance of the present experimental program

It should be emphasized, however, that the CIAD we found remains only a proposal of possible cause of cyclotron emission, until its physical existence is verified experimentally. Feasibility to observe the CIAD radiated from the constrained electrons in laboratory experiments is not clarified yet and left as an open question. To verify the CIAD, the author tries to extend the CRM experiment in vacuum made by Hirshfield and Wachtel [4] to a plasma environment. The purpose of the present experiment is that, in high-density neutralized electron beams such as $\omega_b^2 \gg \tilde{\Omega}^2$, the CIAD with $\omega < \tilde{\Omega} + V_z k_z$ may be observed instead of CRM instability with $\omega > \tilde{\Omega} + V_z k_z$. Although the Hirshfield and Wachtel's short letter paper [4] is believed to be only one reported experiment to verify the CRM instability, it has not been discussed thoroughly by subsequent researchers in literature. This is probably because of terrible brevity of the letter paper. We believe that the present report is the first attempt to explore a possible extension of the experiment to plasma environment.

The author designs and fabricates a plasma-loaded CRM in the TPD-II Machine [12, 13] at National Institute for Fusion Science (NIFS), Japan utilizing as beam source. With increase in density of plasma from TPD-II, the CRM instability may be suppressed and the CIAD may take turn. In other words, frequency of negative absorption observed in vacuum [4] may change from above to below the relativistic electron cyclotron frequency with increase in the beam density in the cavity such that $n \geq 1.5 \times 10^{11}$ cm^{-3}. Analysis, design and preliminary measurements for the fabricated microwave circuits are described. The present efforts are believed to contribute to a deeper understanding and a widened future prospect in physics and engineering of the gyrotrons.

1.4 What is plasma-loaded CRM?

In this report, a design study for experimental verification of the CIAD in plasma-loaded microwave cavity utilizing TPD-II Machine is described. Schematic view of the TPD-II Machine [12, 13] and our constructed plasma-loaded CRM are shown in Fig. 1. In (a), total view of the apparatus is depicted. Plasma is produced by dc helium gas discharge between a hot cathode and grounded anode in TPD-II at the right-side. Plasma is spouted out from an orifice in the anode into left-side plasma container made of quartz pipe in solenoid coils where the plasma-loaded CRM is installed. This portion is evacuated by high speed pumps to remove neutral gases for attaining fully ionized plasma. The plasma column has high density up to 10^{14} cm^{-3}, temperature of a few eV and beam diameter 10 mm.

To detect negative absorption caused by CRM instability or CIAD, a large number of gyrations of the beam inside the cavity is required. The principle of the plasma-loaded CRM is schematically shown in Fig. 1(b). It consists roughly of two different portions: (1) A pair of helical windings called wiggler in this report for creating transverse velocity in the beam at the right-hand side, and (2) the TE_{011} mode cylindrical cavity at the left-hand side. The latter is connected to microwave circuits for detecting negative absorption of incident microwave near 3.45 GHz with power less than 50 mW. The 15 keV electron beam from TPD-II Machine is incident from the right-hand side. The beam, however, has no azimuthal velocity component, namely $V_\theta \simeq 0$. In order to create V_θ for gyrations, the beam is introduced on the axis of the wiggler that produces a helical circularly polarized static magnetic field b_t of the order of 10^{-3} (T) near the axis. Here, b_t can be quite small, because it does not give any energy to the beam. The pitch factor $\alpha = V_\theta / V_z \simeq 0.65$ will be obtained at the exit of the wiggler. The pitch factor α of the beam is further increased by the mirror magnetic field shown in Fig. 1(c) before the incidence on the cavity.

In Fig. 1(c), the calculated distribution of axial magnetic field on the axis of the plasma-loaded CRM is shown. The wiggler and the cavity are located in the axial magnetic field $B_s = 0.03268$ T and $B_0 = 0.1268$ T, respectively. The mirror ratio 3.88 between both of them increases the α above unity that enables many gyrations in the cavity.

It is the purpose of our experimental program to verify a physical cause of cyclotron emission that has not been known up to date. In our plasma-loaded CRM, negative absorption due to the CRM instability is suppressed in high-density beam such as $\omega_b^2 \gg \tilde{\Omega}^2$, namely density $n \gg 1.5\times10^{11}$ cm^{-3}, and the CIAD will take turn.

1.5 Contents of this report

Organization of this report is as follows. The list of contents is shown in page 2. In the sections **2** and **3**, our theoretical and experimental works are presented, respectively. In **2.1**, a defect in all the existing linear dispersion relations of CRM instability is discussed. In **2.2** and **2.3**, our exact linear dispersion relations for cyclotron emission from electron beams neutralized by cold ions are described. In **2.2**, the case of an infinitely thin thickness annular beam is analyzed. The constrained gyration model explained in the Appendix A is used. The derivation of the dispersion relation is summarized in the Appendix B. The results of the numerical analysis are shown in Fig. 4. Somewhat surprisingly, observed instability is not the well-known CRM instability $(\omega > \tilde{\Omega} + V_z k_z)$, but CIAD $(\omega < \tilde{\Omega} + V_z k_z)$ newly found by us. In **2.3**, the case of annular electron beam with small but finite thickness is analyzed. The derivation of the dispersion relation is shortly summarized in the Appendix C. A numerical example of our dispersion relation (C 1) involving both instabilities is shown in Fig. 5. In **2.4**, particle simulation is conducted to elucidate the physical distinction between both instabilities. The equations used in the simulation are listed in the Appendix D. The results are described in some detail in Figs 6-9. The CRM instability and CIAD are caused, respectively, by free and constrained gyrations of the electrons near the cyclotron resonance $\omega \simeq \tilde{\Omega}$.

In **3.1** and **3.2**, respectively, we design (1) a pair of helical windings of wiggler for creating transverse velocity with pitch factor $\alpha \simeq 0.65$ in 15 keV beam, and (2) microwave circuits including the TE_{011} mode cylindrical cavity for detecting negative absorption of incident microwave at 3.45 GHz. Design study of (2) is described in **3.2**. In **3.2.1**, physical interpretation of the previous experiment [4] to detect negative absorption caused by CRM instability in a cavity in vacuum is tried. In **3.2.2**, performance of one-port cavity is analyzed by using scattering matrix theory for understanding the relationship between negative absorption inside the cavity and detected signals in external microwave circuits. In **3.2.3**, expected microwave signals to detect the CIAD in addition to CRM instability are calculated numerically. In **3.2.4**, fabricated cavity and microwave circuits for the plasma-loaded CRM are described.

Lastly, discussion and conclusion are given in **4**. In Appendix A, the physical reason of the constrained gyration model that gives rise to the CIAD is explained. In Appendices B-D, the formulations derived for our theoretical works in section **2** are summarized.

Flow chart of this report is given in page 3 to clarify the logical relationship among various sub-sections. The upper and lower halves of the chart are, respectively, theoretical and experimental works. Arrows mean the logical relationship between motivation and consequence.

2. Theoretical Study on CRM Instability and CIAD

2.1 Conventional erroneous linear dispersion relations for CRM instability

The CRM instability [4-8] has been believed to be caused by the faster branch $\omega > \tilde{\Omega} + V_z k_z$ denoted by +FCM of the fast cyclotron wave $\omega = \tilde{\Omega} + V_z k_z$. It must be emphasized, however, that all the existing linear dispersion relations [5-8] of the CRM instability include unphysical branches unstable at infinite values of axial wavenumber k_z in the slow wave region $(\omega / k_z < c)$ that can never be observed experimentally.

A numerical example of the linear dispersion relation of CRM instability derived by Sprangle and Drobot [5, eq. 1] calculated by us is shown in Fig. 2. Given numerical parameters are indicated in the figure. The growth rate in the fast wave region $(\omega / k_z > c)$ near $k_z = 0$ was believed the

CRM instability. This figure, however, involves unphysical numerical instabilities both sides extending to infinite values of k_z, although the authors erased these unphysical branches without any notice [5, Fig. 4]. Researchers have trusted that the growth rate near $k_z = 0$ is still CRM instability. The fact is as follows: Their physical explanation [5, Fig. 1] of CRM instability was correct, but their relation [5, eq. 1] of CRM was incorrect. Both of them have nothing to do with each other.

The reason why the CIAD was not involved in their dispersion relation [5, eq. 1] of CRM was that the boundary conditions with finite Larmor radius effect at beam-vacuum interface were not analyzed correctly. In order to understand CRM instability physically, one must take into account the logical presence of CIAD that is unavoidable in general whenever a high density beam has boundary. It is quite important to understand the CIAD, a new principle of cyclotron emission, for the development of physics of gyrotrons.

2.2 An exact dispersion relation for infinitely thin thickness annular beam

The model of our analyses is shown in Fig. 3, that is a cross-sectional view of cylindrical waveguide including a concentric LO annular beam in the region II. Here, the regions I and III are vacuum. The axial magnetic field B_0 is in the direction from the sheet to our eyes. Circular arrow means the direction of rotation of electrons and right-hand ciecularly polarized electromagnetic field.

First, we analyze a case that the thickness denoted by Δ of annular beam in the region II is infinitely thin, namely $\Delta \to 0$. In this case, no radial motion of the gyrating electrons is allowed, and they must stay on the original LO circle at any momemt. This strange model is called the constrained gyration model in this peport. The physical reason for the model is explained in the Appendix A.

The derivation of the exact dispersion relation (B 1) for infinitely thin annular beam is summarized in Appendix B. We here describe only the results of numerical analysis. In Figs. 4(a) and (b), the dispersion relation (B 1) is solved numerically for quasi-TE_{11} (Q-TE_{11}, hereafter) mode. Numerical parameters are given in the caption. The strength of B_0 is chosen so that the negative energy wave [14], namely, slow branch of fast cyclotron mode (–FCM) grazes the parabolic curve of TE_{11} mode in empty waveguide. The thin dotted oblique lines in Fig. 4(a), (c) and (e) are light lines in vacuum. The dashed line is FCM, $\omega = k_z V_z + \tilde{\Omega}$, when the space-charge effects are ignored.

In Figs. 4(a) and (b), all terms in surface current density (A 3) are retained while solving the dispersion relation (B 1). In Fig. 4(a), the frequency of radiation is less than the cyclotron frequency $\omega < \tilde{\Omega}$ at k_z=0. The temporal growth rate is depicted in Fig. 4(b). The instability shown in Fig. 4(a) and (b) is named the CIAD. It is clearly shown that the unstable branch is the slower branch –FCM that is different from +FCM in the case of CRM instability as shown in Fig. 2. Somewhat surprisingly, Fig. 4 (a) and (b) for infinitely thin annular beam does not indicate CRM instability.

In Figs. 4(c) and (d), all relativistic terms are ignored approximately in (A 3) by tending $c \to \infty$. In doing so, we exclude azimuthal bunching caused by relativistic effect for CRM instability [3-8]. It is noted that Figs 4(c) and (d) are qualitatively similar to Figs. 4(a) and (b), respectively. Figure 4(c) suggests the non-relativistic nature of the instability shown in Fig. 4(a), because the thick curves of $\mathrm{Re}(\omega)/2\pi$ in both figures are qualitatively similar to each other. The corresponding temporal growth rate shown in Fig. 4(d) becomes doubly peaked because –FCM is intersecting the TE_{11} mode at slightly higher frequency in case of $\gamma_0 = 1$. In this report, the instability observed in Fig. 4(a)-(d) is named the CIAD in fast wave region ($\omega / k_z > c$). This instsbility is smoothly continuing to fast cyclotron instability in slow wave region ($\omega / k_z < c$) of BWOs [9], when the radius of the cylindrical waveguide has a corrugation in the axial direction.

On the other hand, we drop all the non-relativistic terms in (A 3), without legitimacy, to exclude the nonrelativistic effect in Fig. 4(e) and (f). The illogical assumption $c \to 0$ results in radiation

with $\omega > \tilde{\Omega}$ at k_z=0 as shown by thick curves in Fig. 4(e). The corresponding temporal growth rates are shown in Fig. 4(f). Figures 4(e) and (f), drawn through unphysical prosedure from the dispersion relation (B 1), is very similar to conventional linear dispersion relations of CRM obtained by Sprangle and Drobot [5, eq. 1], and by Chu and Hirshfield [6, eq. 8]. In other words, Figs 4(e) and (f) are almost identical to Fig. 2. Their relations include unphysical branches, P_2 and P_2' in Fig. 4(f), that are unstable in the limit of wavenumber $k_z \to \pm\infty$. Their analyses are approximate ones in the sense that either a particular mode was assumed in advance or the boundary conditions with finite Larmor radius effect at beam-vacuum interface were not correctly included. The relativistic Vlasov-Maxwell equations that these authors started to derive the dispersion relations might not be Lorentz invariant.

These classical relations, Figs 4(e) and (f), were undersood to be correct, because the obtained branch of CRM instability P_1 with $\omega > \tilde{\Omega}$ at k_z=0 in Figs 2 and 4(f) was qualitatively identical to the experimental fact $\omega > \tilde{\Omega}$ [4, Fig. 2(a)] and physical interpretation of CRM instability $\omega > \tilde{\Omega}$ [5, Fig. 1]. However, this coincidence cannot justify to ignore the presence of unphysical branches in their dispersion relations. The unphysical branches are the evidence of inadequate derivation of the linear dispersion relations of CRM. Such unphysical instabilities flat for k_z are observed often in numerical analyses, but have never been observed experimentally.

The correct dispersion relation of CRM instability should include radiation of $\omega > \tilde{\Omega} + V_z k_z$ in the fast wave region, and should not include unphysical branches in the slow wave region such as those unstable for k_z infinity. Any instability should be allowed for a limited range of k_z near the intersection of structure mode with a negative energy wave [14] in the beam. More exactly, an upper limit of wavenumber k_z must exist always, above which the interaction is stable.

A correct dispersion relation that includes both CIAD and CRM instability is obtained, if one analyzes a finite-thickness LO annular beam shown in Fig. 3 that allows radial displacement of the electrons, as will be shown in the next sub-section.

2.3 An exact dispersion relation for small but finite thickness annular beam

Next, we analyze the LO annular beam with small but finite-thickness in a cylindrical waveguide shown in Fig. 3. The model of analysis is similar to those by previous researchers [7, 8], but the result is significantly different. We show here a numerical example of our new dispersion relation that includes both CIAD ($\omega < \tilde{\Omega} + V_z k_z$) and CRM instability ($\omega > \tilde{\Omega} + V_z k_z$) of Q-TE_{11} mode at the same time. Some electrons located deep inside the surface of the beam can dislocate freely in radial direction through uniform ions, and result in the CRM instability. The other electrons near the boundary must be constrained from radial movements because of restoring force by neutralizing ions so that the CIAD arises.

We assume again that the regions I and III in Fig. 3 are in vacuum, and the region II is a uniform LO beam. Notations of outer radius r_b^+, inner radius r_b^- and a small thickness $\Delta = r_b^+ - r_b^-$ are used. The rf field components in regions I and III in vacuum can be straightforwardly written in ordinary way using Bessel functions. In Appendix C, the derivation of the linear dispersion relation (C 1) for a small but finite-thickness annular neutralized electron beams is shortly described.

A numerical example of our new linear dispersion relation (C 1) of Q-TE_{11} mode is shown in Fig. 5. Given numerical parameters are: Waveguide radius r_{cav}=1.445 cm, axial magnetic field B_0=0.5 T, beam energy E_b=630 keV, pitch angle of the beam $\alpha = 10$ and beam current I_b=3.864 mA. The resultant radius of LO circle is $r_b = V_\theta / \tilde{\Omega}$=0.677 cm. The thickness of the annular beam is given by $\Delta r = r_b^+ - r_b^- = r_b / 100 = 6.77 \times 10^{-3}$ cm. Figure 5(a) is oscillation frequency $f = \mathrm{Re}(\omega)/2\pi$ (GHz) versus axial wavenumber k_z (cm^{-1}), and (b) is temporal growth rate $\mathrm{Im}(\omega)$ (ns^{-1}) versus k_z (cm^{-1}). Thin solid parabolic curve in Fig. 5(a) is TE_{11} mode in empty cylindrical waveguide. The dashed straight line is fast electron cyclotron mode $\omega = \tilde{\Omega} + V_z k_z$ for $\omega_b = 0$.

It is clearly shown in Fig. 5(a) and (b) that the CIAD with $\mathrm{Re}(\omega) < \tilde{\Omega} + V_z k_z$ and the CRM instability with $\mathrm{Re}(\omega) > \tilde{\Omega} + V_z k_z$ denoted, respectively, by S and T are observed at the same time. This is because electrons with both free and constrained gyrations coexist in the finite-thickness annular LO beam. Here, $\tilde{\Omega} = 3.9 \times 10^{10}$ Hz, and $\omega_b = 10^9$ Hz. It is noted that the CIAD can be observed although $\omega_b^2 < \tilde{\Omega}^2$ in this case. If one of the extreme conditions, $\omega_b^2 \ll \tilde{\Omega}^2$ and $\omega_b^2 \gg \tilde{\Omega}^2$, were chosen, the CRM instability and the CIAD will be exclusively observed, respectively.

The previous analysis for infinitely thin-thickness annular beam in Fig. 4 exhibited CIAD, but no CRM instability was included. In the case of CRM instability, azimuthal bunching of freely gyrating electrons is always accompanied by radial excursion. On the other hand, radial displacements of the gyrating electrons are prohibited by restoring force from cold and localized ions in the constrained gyration model given in the Appendix A. The CRM instability is suppressed and the CIAD takes turn to arise in high density beam.

Figure 5 supports the co-existence of the CRM instability and the CIAD, when some electrons are free to gyrate and others are constrained because of the presence of the fixed boundaries at beam-vacuum interface. Figure 5 is the first example of an exact linear dispersion relation of CRM in which the numerical (unphysical) instability at k_z infinity observed in the conventional relations [5-8] is removed. These unphysical modes are now replaced by two neutral branches near the fast electron cyclotron mode $\omega = k_z V_z + \tilde{\Omega}$ for $\omega_b = 0$ in the slow wave regions, $|\omega / k_z| < c$, as shown in right-top and left-bottom corners in Fig. 5(a).

2.4 Numerical particle simulation for clarifying two principles of cyclotron emission

In Figs 6-9, we carry out a particle simulation to elucidate the subtle distinction between the CRM instability and the CIAD [10].

In Fig. 6, bunching of the 16 test electrons is tracked numerically by solving a relativistic equation of motion of electrons given by (D 1) in Appendix D for six typical cases of $\omega / \tilde{\Omega}$ and beam density *n*. The 6th order Runge-Kutta method [16] is used to track the electron gyration in a right-hand circularly polarized plane electromagnetic field. Interactions among the electrons are ignored.

Given parameters are as follows: A mildly relativistic case of initial electron energy $E_b = 100$ keV, pitch factor $\alpha = 1.0$ and constant rf field $E_{rf} = 3 \times 10^5$ V/m. The amplitude E_{rf} of rf fields in (D 1) is a given parameter and assumed to be constant during the numerical simulation. Accordingly, the total energy in the interaction between the 16 electrons and rf field is not conserved. We do not intend to calculate exactly the equation at the nonlinear stage of the electron motion, because constant amplitude E_{rf} is assumed in (D 1). We mostly confine ourselves to the initial linear periods within 20 gyrations of the electrons, in order to investigate in detail the existence of the CIAD in addition to the CRM instability distinguished in [9]. After a number of rotations of the rf field, the average energy gain of all the 16 electrons, $\langle \delta\gamma \rangle = \langle \gamma - \gamma_0 \rangle$, is calculated. Here, γ and γ_0 are, respectively, the relativistic factor after gyrations and its initial value. Radiation from gyrating electrons can be expected, if $\langle \delta\gamma \rangle < 0$.

In Fig. 6(a)-(f), thin circle in each figure is the LO circle on which 16 electrons are located with equal separation initially. The upward arrow at the center of each LO circle is the direction of the instantaneous rf electric field at the initial moment and after the rotations. The direction of magnetic field B_0 is from the sheet to our eyes in Fig. 6, namely the electrons and the rf field are rotating counterclockwise with angular frequency $\tilde{\Omega}$ and ω, respectively. In each figure, the uniform rf electric field in the upward direction as shown by the arrow exerts a force in downward direction to

every gyrating electron. Small black and white circles are, respectively, the locations of the electrons that lose and gain net kinetic energy against the rf field.

A neutral bunching case of $\omega/\tilde{\Omega}=1.0$ and $n=10^{10}$ cm^{-3} of free gyration after 11 rotations of rf field is shown in Fig. 6(a). The value $\langle\Delta\gamma\rangle=1.2183\times10^{-3}>0$ suggests that the interaction is stable. Since there are no sufficient ions to prevent the radial displacements, free electron gyration is possible, and the electrons can deviate from the original LO circle freely. It should be noted that bunched electrons at right and left sides of the arrow are decelerated and accelerated, respectively, by the rf electric field, because the electrons are gyrating counterclockwise. So, the condition $\langle\Delta\gamma\rangle<0$ for instability is met, if the bunched electrons are located at the right side of the upward arrow and are decelerated secularly by the rf field both in free and constrained gyration models.

In Fig. 6(a), the electrons are at rest initially in a rotating frame with ω, since $\tilde{\Omega}=\omega$. After a number of rotations of rf field, the black electrons located at the right side of the upward arrow lose kinetic energy, and are found inside the LO, whereas the white electrons at the left side of the arrow gain kinetic energy from the rf field and are found outside the LO. This is because the Larmor radius $v_\theta/\Omega\neq r_b$ of each electron changes with change in the instantaneous kinetic energy, where $\Omega=eB_0/m\gamma$ is the changed electron cyclotron frequency, and r_b is the initial radius of LO.

In Fig. 6(a), the upward rf field accelerates the electrons downward at the left side of the arrow in the direction of gyration, and as a result, causes increase in v_θ and γ. Then, Ω decreases from its initial value $\tilde{\Omega}=eB_0/m\gamma_0$, namely $\Omega<\tilde{\Omega}$. Since the free electrons gyrate with angular frequency $\partial\theta/\partial t=\dot{\theta}=\Omega$, the gyration of the electrons retard clockwise from the initial value of angular frequency $\tilde{\Omega}$, despite that v_θ also increases from the initial value. The retarded gyration through excursion on the detour path of the electrons from LO is the physical reason of CRM instability. On the other hand, the same upward rf field decelerates gyrating electrons located at the right side of the arrow, and as a result, $\Omega>\tilde{\Omega}$. Since the angular frequency $\partial\theta/\partial t=\dot{\theta}=\Omega$ increases, the positions of these electrons near the LO proceed counterclockwise and slide upwards after several rotations of rf field. In the case of free gyrations, key point for arising the azimuthal bunching after several rotations is not the change in the velocity v_θ, but the change in Ω. The neutral bunching in Fig. 6(a) arises at the top of the LO, accordingly. Energy exchange between the electrons and the rf field is expected to be very small, because the bunching occurs near a neutral point where no rf field in azimuthal direction is present. This azimuthal bunching disappears in a non-relativistic beam, $\gamma_0=1$.

Another neutral bunching case of $\omega/\tilde{\Omega}=1.0$ for constrained electrons neutralized by ions with density $n=10^{14}$ cm^{-3} after 7 rotations of rf field is shown in Fig. 6(b). Other given parameters are identical to Fig. 6(a). The electrons are almost completely constrained on the original LO circle, and the value of $\langle\Delta\gamma\rangle=2.4091\times10^{-4}>0$ means again absence of instability. The bunching happened at the top of the LO circle in Fig. 6(a), whereas it takes place at the bottom of the LO circle in Fig. 6(b). The constrained electrons circulate counterclockwise with angular frequency $\partial\theta/\partial t=\dot{\theta}=v_\theta/r_b$, where r_b is constant in the case of constrained gyration. For constrained electrons in Fig. 6(b), angular frequency $\dot{\theta}\neq\Omega$ in general. This is because the centrifugal force on the electrons must be balanced not only by the Lorentz force due to axial magnetic field B_0 but also by the restoring force from neutralizing ions against the deviation from the original LO.

In the frame rotating with rf electric field, all the electrons are initially at rest, because $\omega=\tilde{\Omega}$ in Fig. 6(b). The electrons left to the upward arrow gain kinetic energy from the rf field, and their v_θ and γ increase. Since the Larmor radius must remain to the initial value r_b in the

constrained gyration model, an increase in v_θ causes an increase in $\dot{\theta}$, and the increase in γ from γ_0 results in $\Omega < \tilde{\Omega}$, namely, $\dot{\theta} > \tilde{\Omega} = \omega > \Omega$. Thus, these electrons that were initially at rest in the rotating frame, start to proceed counterclockwise towards the bottom of the LO circle after several rotations of rf field.

On the other hand, the electrons located at the right to the arrow lose kinetic energy, and their v_θ and γ decrease. The decrease in v_θ causes a decrease in the angular frequency $\dot{\theta}$, and the decrease in γ from γ_0 results in $\Omega > \tilde{\Omega}$. These electrons start to retard clockwise towards the bottom of the LO after some rotations, because $\dot{\theta} < \tilde{\Omega} = \omega < \Omega$. In the case of constrained gyration, key point for arising the azimuthal bunching after several rotations is not the change in Ω, but the change in the velocity v_θ. Consequently, neutral bunching takes place at the bottom of the LO circle in Fig. 6(b). Energy exchange between the electrons and the rf field is again little, because the bunching occurs near a neutral point where no rf field in azimuthal direction is present. This bunching can exist even in the non-relativistic limit, $\gamma_0 = 1$.

The electron bunching near neutral point arises very differently in Fig. 6(a) and (b). The difference in locations of neutral bunching in Fig. 6(a) and (b) gives rise to the distinction between the CRM instability and the CIAD.

Next, we consider the cases of $\omega/\tilde{\Omega} \neq 1.0$ in which instability can occur. A free gyration case with $n = 10^{10}$ cm^{-3}, $\omega/\tilde{\Omega} = 1.04$ and after 15 rotations of rf field is shown in Fig. 6(c). Other given parameters are identical to Fig. 6(a). The value of $\langle \Delta\gamma \rangle = -5.5376 \times 10^{-3} < 0$ means the CRM instability. Because $\omega > \tilde{\Omega}$, the rotating rf electric field shown by the upward arrow overtakes counterclockwise slowly the gyrating electrons. The neutral bunching at the top in Fig. 6(a) retards clockwise to the right side of the arrow where the bunched electrons are decelerated, because the downward force is in opposite direction to the cyclotron motion. They secularly lose kinetic energy against the rf electric field so that well-known CRM instability takes place. This physical explanation is identical to that was correctly given by Sprangle and Drobot [5, Fig. 1].

In Fig. 6(e), another free gyration case $n = 10^{10}$ cm^{-3}, $\omega/\tilde{\Omega} = 0.96$ and after 14 rotations of rf field is shown. Other given parameters are identical to Fig. 6(a). The value of $\langle \Delta\gamma \rangle = 6.2625 \times 10^{-3} > 0$ means that the interaction is stable. The neutral bunching at the top in Fig. 6(a) slides counterclockwise towards left side of the upward arrow, because $\omega < \tilde{\Omega}$. The bunched electrons at the left side of the arrow are accelerated downwards in the same direction as the gyration so that they get kinetic energy secularly from the rf electric field. This is a case of stable bunching.

A constrained gyration case of $n = 10^{14}$ cm^{-3}, $\omega/\tilde{\Omega} = 0.96$ and after 7 rotations of rf field is shown in Fig. 6(f). Other given parameters are identical to Fig. 6(a). The value of $\langle \Delta\gamma \rangle = -2.0818 \times 10^{-3} < 0$ reveals the presence of the CIAD. The gyrating electrons overtake slowly counterclockwise the rf field, because $\omega < \tilde{\Omega}$. The neutral bunching at the bottom in Fig. 6(b) proceeds counterclockwise toward the right side of the upward arrow. The bunched electrons are decelerated downwards in opposite direction to circulation so that they give energy secularly to the rf electric field. This is the physical reason of CIAD.

Another constrained gyration case for $n = 10^{14}$ cm^{-3}, $\omega/\tilde{\Omega} = 1.04$ and after 7 rotations of rf field is shown in Fig. 6(d). Other given parameters are identical to Fig. 6(a). The value of $\langle \Delta\gamma \rangle = 1.9157 \times 10^{-3} > 0$ means that the interaction is stable. The neutral bunching at the bottom in Fig. 6(b) retards clockwise towards left side of the upward arrow, because $\omega > \tilde{\Omega}$. The bunched electrons are accelerated downwards in the direction of circulation so that they get kinetic energy secularly from the rf electric field. This is another case of stable bunching. These are all the

explanations of the physical mechanism of the CRM instability and the CIAD. The former and the latter instabilities, respectively, disappears and survives in non-relativistic limit, $\gamma_0 = 1$, as was clarified in the above physical explanations.

Temporal changes in the relative energy gain $<\delta\gamma>/\gamma_0$ of the 128 electrons versus normalized time $\tau = t\tilde{\Omega}/2\pi$ =0 to 15 are presented in Fig. 7, for various values of beam density *n* up to 10^{15} cm^{-3}. Here, τ is time normalized by time of gyration. Mildly relativistic beam energy E_b=100 keV, pitch factor $\alpha = V_\theta / V_z = 1.0$ and constant rf field E_{rf}=3×10^5 V/m are assumed. Dashed and dotted curves are for the free gyration case *n*=0 and the constrained case *n*=10^{15} cm^{-3}, respectively. Oscillation can occur, if $\langle\delta\gamma\rangle < 0$. In Fig. 7(a), $\omega/\tilde{\Omega}$ =0.96 is given. The CIAD is observed for $n > 3\times10^{12}$ cm^{-3}, namely, $\omega_b > 7.5\times10^{10}$ Hz whereas $\tilde{\Omega}$ =1.5×10^{11} Hz. This value of $n = 3\times10^{12}$ cm^{-3} does not change, when E_{rf}= 3×10^4 V/m is given. In Fig. 7(b), $\omega/\tilde{\Omega}$ =1.04 is chosen, and the CRM instability is observed for $0 \le n < 2\times10^{12}$ cm^{-3}, namely $\omega_b < 6.1\times10^{10}$ Hz whereas $\tilde{\Omega}$ =1.5×10^{11} Hz. It is shown in Fig. 7(a) and (b) that the CIAD and the CRM instability dominate, respectively, for $\omega_b^2 \gg \tilde{\Omega}^2$ and $\omega_b^2 \ll \tilde{\Omega}^2$ as are designated by the boldface letters.

Relative energy gains $<\delta\gamma>/\gamma_0$ of the 128 electrons after normalized time $\tau = 10$ of gyrations versus $\omega/\tilde{\Omega}$ for the mildly and weakly relativistic cases, 100 keV and 10 keV, are depicted, respectively, in Fig. 8(a) and (b). A constant E_{rf}=3×10^4 V/m and $\alpha = V_\theta / V_z = 1.0$ are given. Oscillation can occur for $\langle\delta\gamma\rangle < 0$. In Fig. 8(a), mildly relativistic case E_b=100 keV is shown. The CIAD is observed for $n > 3\times10^{12}$ cm^{-3}, namely, $\omega_b > 7.5\times10^{10}$ Hz and for $\omega/\tilde{\Omega}$ <1, whereas $\tilde{\Omega}$ =1.5×10^{11} Hz. The maximum decrease in $<\delta\gamma>/\gamma_0$ is observed near $\omega/\tilde{\Omega}$ =0.96. The CRM instability is found for $n < 3\times10^{12}$ cm^{-3} and for $\omega/\tilde{\Omega}$ >1. The maximum decrease in $<\delta\gamma>/\gamma_0$ is obtained near $\omega/\tilde{\Omega}$ =1.04. In Fig. 8(b), weakly relativistic case E_b=10 keV is shown. The CIAD is observed for $n > 10^{12}$ cm^{-3} and for $\omega/\tilde{\Omega}$ <1. The maximum decrease in $<\delta\gamma>/\gamma_0$ is again obtained near $\omega/\tilde{\Omega}$ =0.96. The CRM instability is not observed for any density *n* and in vacuum near $\omega/\tilde{\Omega} = 1.04$.

Temporal changes in the relative energy gain $<\delta\gamma>/\gamma_0$ of the 128 electrons from $\tau = 0$ to 15 are shown in Fig. 9 for various values of beam energy $E_b \le 700$ keV. A constant rf field amplitude E_{rf}= 3×10^5 V/m and $\alpha = V_\theta / V_z = 1.0$ are assumed. Oscillation can occur, if $\langle\delta\gamma\rangle < 0$. In Fig. 9(a), $\omega/\tilde{\Omega}$ =0.96 and $n = 10^{14}$ cm^{-3} are assumed. The CIAD is observed for E_b< 500 keV, and this upper limit of E_b for CIAD is found to increase for $n > 10^{14}$ cm^{-3}. The strength of restoring force that is proportional to *n* shown in (D 1) becomes insufficient to constrain the gyration of electrons for extremely large values of E_b. In other words, the CIAD disappears for ultra-relativistic electron beams. On the other hand, in Fig. 9(b), $\omega/\tilde{\Omega}$ =1.04 and $n = 10^{10}$ cm^{-3} are assumed. The CRM instability is enhanced unlimitedly with increase in E_b.

Numerical results shown from Figs 6-9 are summarized as follows. First of all, the CIAD and the CRM instability are observed exclusively for $\omega < \tilde{\Omega}$ and $\omega > \tilde{\Omega}$, respectively. The maximum decreases in average energy of the electrons are found, respectively, near $\omega/\tilde{\Omega}$ =0.96 and 1.04 for these two instabilities as shown in Fig. 8. These values of $\omega/\tilde{\Omega}$ at the maximum decrease do not change appreciably for a variety of given parameters. For mildly relativistic beam of 100 keV, both the CIAD and the CRM instability are observed for various *n* as shown in Fig. 7(a). It is emphasized that the CIAD and the CRM instability are observed above and below beam density $n \simeq 10^{12}$ cm^{-3},

respectively. Both instabilities are not observed at the same time for a given beam density. In other words, the radiation from the CRM instability ($\omega > \tilde{\Omega}$) ceases, and the CIAD ($\omega < \tilde{\Omega}$) takes turn to arise with gradual increase in the beam density across $n \simeq 10^{12}$ cm^{-3}. The CIAD can be observed only for the cases roughly n>10^{12} cm^{-3} for a wide range of given parameters in our simulation. For a weakly relativistic beam of 10 keV, the CRM instability is altogether suppressed as shown in Fig. 8(b). The CRM instability is based on relativistic changes in mass of the electrons, and it disappears for low beam energies $E_b \leq 10$ keV, whereas the CIAD is observed in non-relativistic limit, $\gamma_0 = 1$, even for low energy $E_b \leq 10$ keV, if n>10^{12} cm^{-3}. On the other hand, the CIAD is suppressed for large values of E_b, as shown in Fig. 9(a).

3. Design Study of Plasma-Loaded CRM in TPD-II Machine

3.1 Wiggler windings for creating 15 keV mono-energetic spiral electron beam

Most common way to produce mono-energetic spiral electron beam is magnetron injection gun (MIG) utilized in gyrotrons [2]. However, the MIG is the one of the most elaborate issues in construction and operation of any gyrotron, and it is not easily available in our experiment using the TPD-II Machine. Moreover, we are going to construct a gyrotron itself, if we use MIG. Here, we follow a method of wiggler to create spiral beam by using a pair of helical windings and mirror magnetic field before the incidence on the cylindrical cavity [4, 17].

We have assembled dc high-voltage source up to -20 kV for applying a typical voltage of -15 kV to the flowing plasma from TPD-II. The accelerated beam-plasma by a pair of mesh electrodes has thermal broadening at a temperature of a few eV and we must assume $V_\theta \simeq 0$ initially. To produce mono-energetic spiral beam, a wiggler with bifilar helical windings is designed.

The relativistic factor in case of beam energy $E_b = 15$ keV is given by $\gamma_0 = 1 + eE_b / mc^2 = 1 + 15/511 = 1.03$ and $V_\theta \simeq 0$. Then, $V_z = \beta c = 7.11 \times 10^7$ m/s. Accordingly, the electrons execute right-hand spiral motions of infinitely small Larmor radii with axial pitch length V_z / f_c. Here, f_c is the cyclotron frequency at the location of wiggler windings. If the pitch length λ_w of the right-hand circularly polarized dc magnetic field b_t generated by the wiggler is equal to V_z / f_c, the electrons are accelerated in azimuthal direction secularly by the Lorentz force $-e\vec{v}_z \times \vec{b}_t$ at the expense of their axial velocity. The amplitude of the helical magnetic field b_t is roughly evaluated as follows. The relativistic motion of an electron is given by,

$$\frac{\partial \vec{v}_\perp}{\partial t} = -\frac{e}{\gamma_0 m} \vec{v}_z \times \vec{b}_t , \qquad (1)$$

where γ_0 is kept constant. Integrating the equation (1) in time, one obtains $v_\perp \simeq (e/\gamma_0 m) b_t L$, where $L = \int V_z dt$ is total length of the wiggler. We assume typical values of $L = 0.4$ m and $v_\perp = V_z / 4$ from our experimental view point. The required b_t is calculated to be 2.6 Gauss. It is noted that the value of b_t can be quite small to increase $\alpha = V_\theta / V_z$ significantly, because no energy exchange is present between the helical magnetic field b_t and the electrons.

Exact value of required b_t is evaluated by numerically tracking the motions of 16 electrons initially located on a circle of Larmor radius with equal separation by using the equation (1). Wiggler is designed to be immersed in the axial magnetic field $B_s = 0.03268$ T that corresponds to $f_c = 8.89 \times 10^8$ Hz for the 15 keV beam without gyration from TPD-II. Here, the value of B_s is chosen so that the pitch length $\lambda_w = V_z / f_c = 8$ cm is available, that is a convenient value from experimental point of view.

In Fig. 10, the transverse circularly polarized magnetic field b_t is produced on the axis by the bifilar helical windings with dc current I_{tot} in opposite direction with each other. In (a), the windings create $\vec{b}_t$ denoted by short thick arrows on the z axis. In (b), the change in $\vec{b}_t$ in the axial direction is explained. The points P, Q and R in (b) correspond, respectively, to the short vectors in (a). The electron beam propagates from left to right sides with velocity $V_z = 7.11\times10^7$ m/s, and accelerated by Lorentz force $-e\vec{v_z}\times\vec{b}_t$ secularly in the azimuthal direction.

The relation between b_t (Gauss) on the axis and the current I_{tot} (A) in the double helixes is formulated by Kincaid [18] as,

$$b_t = \frac{0.8\pi I_{tot}}{\lambda_w}\left[kaK_0(ka) + K_1(ka)\right], \qquad (2)$$

where $k = 2\pi / \lambda_w$, λ_w is pitch length of the windings in cm, a is the radius of the helix in cm, K_0 and K_1 are modified Bessel functions in the second kind. Here, the cross-sectional area of the conductor of windings has been assumed to be infinitely small. It is generally shown from (2) that b_t is large for $\lambda_w \simeq a$, and it becomes small for $\lambda_w \ll a$ and $\lambda_w \gg a$.

The numerical results of b_t versus λ_w are calculated from (2) as shown in Fig. 11 for three values of outer radius a of quartz pipe and for the current $I_{tot} = 60$ A. This value of I_{tot} is the maximum value of the dc current source available in our experiment. Here, Q-24, Q-30 and Q-36 are candidates of product number of quartz pipe through which the beam-plasma column from the TPD-II Machine with typical radius 0.5 cm penetrates on the axis and enter into the cylindrical cavity. The white circle on the pipe Q-30 with $a = 1.775$ cm is the best choice in our experiment. The helical magnetic field $b_t = 12.55$ Gauss is obtained by $I_{tot} = 60$ A, when the pitch length $\lambda_w = 8$ cm of wiggler is chosen.

In Fig. 12, changes in pitch factor $\alpha = V_\theta / V_z$ versus axial position z (m) are calculated for various values of helical magnetic field b_t (Gauss). Other given parameters are beam energy E_b=15 keV, helix pitch $\lambda_w = 8.0$ cm, axial magnetic field B_s=0.03268 T and α (initial)=0.001. Here, motion of 16 electrons on the initial Larmor radius $r_b = V_\theta / \tilde{\Omega}$ with equal separation is calculated numerically by using 6th order Runge-Kutta method [16]. The averaged value α is plotted in Fig. 12. The reason why we calculate the average value of trajectories of 16 electrons is that different initial positions and the velocities of an electron result in different trajectories. It is found, however, that the trajectories are not very different from each other, because $V_\theta \simeq 0$ initially, and the original Larmor radius is quite small. White circle is our chosen parameters. To produce $b_t = 8$ Gauss on the axis, current $I_{tot} = 40$ A is enough as shown in Fig. 12. The designed value of b_t is very small such as $b_t / B_s = 0.024$. Because of this large difference between b_t and B_s, the temporal ripples in the coil currents for the latter may cause a trouble in the operation of our plasma-loaded CRM.

The designed wiggler is a pair of four turn bifilar conductors with pitch length $\lambda_w = 8.0$ cm, radius $a = 1.775$ cm and total length $L = 32$ cm. The larger the value of b_t, the better to attain a large value of pitch factor α as shown in Fig. 12. However, the peak of α for b_t larger than 8 Gauss in Fig. 12 arises at a shorter axial position than $L = 32$ cm. The design will become less reliable, if turn numbers less than four is chosen. So, pitch factor $\alpha = V_\theta / V_z = 0.65$ will be an upper limit in our design of wiggler.

It may be possible, in principle, to increase further the value of α, if a tapered wiggler were

designed. It is found, however, that gradual changes in λ_w or in B_s in axial direction result in quite complicated performances of attainable larger α values. In our experiment, we limit ourselves to use the uniform wiggler, and no further efforts have been made. Instead, the obtained α can be increased further, by transmitting the beam through the mirror field shown in Fig. 1(c) from B_s=0.03268 T at the wiggler to another axial field B_0=0.1268 T at the cylindrical cavity. The mirror ratio is $B_0 / B_s = 3.88$, and α=1.28 will be obtained at the cavity, accordingly.

Erroneous changes in α from the designed value α=0.65 are examined, when one of λ_w, B_s, α (initial) and E_b is deviated from the designed value in Figs 13-16.

In Fig. 13, erroneous changes in attainable pitch factor α versus axial position are calculated for various values of helical pitch length $\lambda_w = 7 \sim 9$ cm. Other given parameters are: Helical magnetic field $b_t = 8$ Gauss, beam energy $E_b = 15$ keV, $B_s = 0.03268$ T and α (initial)=0.001. Thick dashed curve $\lambda_w = 8$ cm is our choice. We have assumed that the cross section of the winding is infinitely small, however, practically a copper conductor with diameter 4 mm is used for the helical windings. Errors in axial location of current flow would be ± 2 mm, and $\lambda_w = 7.8 - 8.2$ cm and $\alpha = 0.58 - 0.73$ indicated by two horizontal dashed lines in Fig. 13 would be unavoidable experimentally. On the other hand, axial length $L = 0.32$ m includes errors on the order of the radius $a = 1.775$ cm of the helical windings that is shown by two vertical dashed lines. The square shaped region formed by four dashed lines in Fig. 13 would be a range of errors in the chosen parameters in our experiment.

In Fig. 14, erroneous changes in pitch factor α versus axial position are calculated for various values of axial magnetic field B_s. Other given parameters are: Helical magnetic field $b_t = 8$ Gauss, beam energy $E_b = 15$ keV, helical pitch length $\lambda_w = 8$ cm and α (initial)=0.001. Thick dashed curve is chosen. Local inhomogeneity in axial magnetic field B_s from the designed value $B_s = 0.03268$ T would be a serious problem expected in our experiment. Erroneous changes in attained pitch factor $\alpha = 0.52 - 0.83$ would be unavoidable experimentally caused by errors in $B_s = 0.031 - 0.034$ T indicated by two horizontal dashed lines in Fig. 14. On the other hand, axial length $L = 0.32$ m includes errors on the order of $a = 1.775$ cm that is shown by two vertical dashed lines. The square region formed by four dashed lines in Fig. 14 would be the range of errors in the chosen parameters in our experiment. This square is adopted to be the region of errors in the designed parameters in Table 1 afterward, since it is larger than that in Fig. 13.

In Fig. 15, increase in pitch factor α versus axial position is calculated for various initial values of α. Other given parameters are indicated in the figure. The attained α is found to become independent from the initial values after a few gyrations, if α (initial) $\ll 1$. The production of mono-energetic spiral electron beam by means of the present helical wiggler windings has an outstanding advantage that attainable α is free from initial velocity distribution of incident beam.

In Fig. 16, erroneous changes in pitch factor α versus axial position are calculated for three values of beam energy E_b. Other given parameters are: Helical magnetic field $b_t = 8$ Gauss, helical pitch length $\lambda_w = 8$ cm, magnetic field $B_s = 0.03268$ T and α (initial)=0.001. Thick dashed curve is chosen, and white circle is chosen parameters. Since the dc high-voltage source has a large power capacity larger than 100 W, no serious ripples in the dc voltage is expected. However, we have no experience to accelerate the beam up to $E_b = -15$ keV, especially high-density beams such as $n \geq 10^{12}$ (cm^{-3}), and attained value of beam energy is unknown at this moment.

Blewett and Chasman [19] derived an expression the magnetic field $b_t(r)$ as a function of radial position off axis as,

$$b_t(r) \propto I_0(kr) - I_1(kr)/kr = 1 + (3/8)(kr)^2 \simeq 1. \quad (3)$$

Because $k = 2\pi/\lambda_w = 0.79$ cm^{-1}, $r \le 0.7$ cm and $(kr)^2 \le 0.3$, the radial changes in b_t would not be a serious problem in our experiment with beam-plasma column from the TPD-II Machine.

Designed beam parameters versus axial position are summarized in Fig. 17. Wiggler windings are installed in the axial position $0 \le z \le 0.32$ m. Pitch length of spiraling electrons decreases from the initial value 8.0 cm. The Larmor radius increases up to 0.7 cm at z=0.32 m.

3.2 Microwave circuits including cavity

3.2.1 Interpretation for detected negative absorption in a cavity [4]

Our experiment in plasma-loaded CRM-CIAD is motivated by the classic experiment of Hirshfield and Wachtel [4] half a century ago for detecting negative absorption in a cavity caused by CRM instability due to low-current spiraling beams in vacuum. We try to extend their experiment to plasma environment. The purpose of our experiment is that, in high density neutralized electron beams such as $\omega_b^2 \gg \tilde{\Omega}^2$, the CIAD with $\omega < \tilde{\Omega} + V_z k_z$ may be observed instead of the CRM instability with $\omega > \tilde{\Omega} + V_z k_z$.

In Fig. 18, an oscilloscope trace in Fig. 2(a) in [4] is quoted that was believed to be the evidence of negative absorption in a microwave cavity caused by CRM instability. However, the principle and result of their microwave measurement in Fig. 18 were not described in detail. In fact, their ingenious and pioneering letter paper [4] is too short for me to follow up the experimental procedure, and I only can understand in some detail what they observed after referring the Ph. D. thesis of Wachtel [20] and references therein. Let me try to summarize my limited understanding shortly. Note that the vertical axis in Fig. 18 is reflected power $|R|^2 > 0$ from the one-port cavity in upward direction. The levels $|R|^2 = 0$ and 1 of the detected power were not indicated. The zero level is supposed to be somewhere below the trace in Fig. 18.

The frequency of input microwave from cw klystron was adjusted at the center of resonance of the empty cavity at 5.8 GHz, so that $|R_{\max}|^2$ was minimized, and axial magnetic field was swept in the horizontal axis. Here, $R_{\max}$ is the reflection coefficient at the peak of the resonance of the cavity. They limited themselves to the incident beam currents sufficiently small so that the resonant frequency did not change appreciably from the value of empty cavity. When the beam without proper wiggler current was incident, only positive absorption at right-side denoted by P was observed. No cyclotron resonance was observed, since transit time of the electrons through the cavity was too short.

As will be shown in Fig. 21 afterward, $|R_{\max}|^2$ increases with increase in the round-trip attenuation α of microwave inside the cavity with under-coupling $0 < s < 1$, because of additional loss by cold electrons. Here, $s = Q_u/Q_e \propto 1/\alpha$ is the coupling factor between the cavity and the microwave circuits, Q_u and Q_e are, respectively, the unloaded Q value and the external Q value, as will be defined afterward. The latter Q_e is a constant of empty cavity. Decreased positive absorption results in a decrease in α and an increase in s. So, $|R_{\max}|^2$ decreases, if $0 < s < 1$. It is assumed that the verification of their negative absorption (exactly, decreased positive absorption) in Fig. 18 was made under the region $0.15 < s < 1.0$.

In Fig. 18, both the negative absorption denoted at N due to energetic spiraling electrons and the positive absorption P due to cold electrons were observed only when the beam with wiggler currents within a small appropriate range was incident. There are electrons with two energies in the cavity at the same time, cold ones E_b=0 and energetic ones E_b=5 keV. The former results in positive absorption at the peak P, and the latter causes negative absorption N.

The authors indicated that, in Fig. 18, the coupling factor of the cavity was $s = 0.15$. Resultantly, $R_{\max} = -0.74$ in Fig. 21 that will appears afterward. The horizontal line extending toward both left and right sides in Fig. 18 was the level of signal $|R_{\max}|^2 = 0.55$ that was reflected power when no beam is incident. The peak value of their positive absorption at P and negative absorption at N will be, respectively, within the ranges $0.55 < |R_{\max}|^2$ and $0 < |R_{\max}|^2 < 0.55$. Exactly speaking, the point N is not the negative absorption in our terminology shown afterward in Figs 20 and 21, but a "decreased positive absorption" caused by a decrease in positive attenuation α due to spiraling energetic electrons.

In Fig. 18, the magnetic field for $\omega = \tilde{\Omega}$ at 5.8 GHz was $B_0 = 0.2091$ T for their 5 keV beam, and the negative absorption (namely, decreased positive absorption) N was observed at the low-field side. Namely, observed negative absorption for $\omega > \tilde{\Omega}$ was the evidence of the CRM instability. If the CIAD were detected, the negative absorption would have been observed at high-field side $\omega < \tilde{\Omega}$. In principle, there are no other means to distinguish the CRM instability and the CIAD, but to distinguish $\omega > \tilde{\Omega}$ and $\omega < \tilde{\Omega}$. This is because the two instabilities are very similar to each other as shown in Fig. 6.

The authors [4] assumed an analogy that the signal in Fig. 18 measured by the power sensitive crystal detector was proportional to the real part of plasma conductivity. Namely, the detected signal was proportional to the collision frequency ν_c of electrons in discharge plasmas, if the change in $|R_{\max}|^2$ due to the cyclotron resonance was much smaller than $|R_{\max}|^2 = 0.55$ [21, Fig. 3]. The trace in Fig. 18 was assumed to be directly proportional to the theoretical expression for power of the positive and negative absorptions [3, eq. 8]. Since the authors [4] did not indicate the scale of $|R|^2 = 0$ and 1 in the vertical axis for the trace in Fig. 18, the readers cannot confirm how their assumption was satisfied. Their assumption is valid, if and only if the coupling factor s is within a range $0 < s < 1.0$. In general, their small change approximation is unnecessary, if an analysis on the relationship between the cavity and the external circuit shown in the next sub-section **3.2.2** is made. In general, however, the relationship between α and $|R_{\max}|^2$ is complicated.

Although Fig. 18 seems to detect the CRM instability, questions still arise. The trace in Fig. 18 without scale in vertical axis was only one result they showed for the evidence of negative absorption. Question arises: "Is the waveform near N in Fig. 18 somewhat similar to phase sensitive pattern [21, Fig. 2(b)] rather than power sensitive pattern [3, Fig. 1], because the trace is roughly symmetrical to horizontal line?" "How does change the trace, when the reference signal from the arm of matched load is changed?" In order to understand Fig. 18 more exactly, we need to see a few more examples with scale in vertical axis of negative absorption obtained under different conditions. The present experimental program will respond to such questions or necessities.

Unfortunately, the authors [4] did not publish any full paper to explain the details of their experiment. The letter paper did not arouse further efforts by other researchers to extend the subject of CRM toward high power microwave sources. The present report seems to be the first attempt to explore an extension of the experiment in vacuum to plasma circumstance.

3.2.2 Analysis of one-port cavity including negative absorption caused by CRM or CIAD

Scattering matrix for one-port cavity shown in Fig. 19 was given by a classic textbook by Altman [22] as,

$$\begin{aligned} b_1 &= \sqrt{1-h^2}\,a_1 + jha_2, \\ b_2 &= jha_1 + \sqrt{1-h^2}\,a_2, \\ b_3 &= -a_3, \\ a_3 &= b_2 e^{-(\alpha/2 + j\theta)}. \end{aligned} \tag{4}$$

Here, we assume that the cavity is straight and the cross section is uniform, for simplicity. We limit ourselves to the fundamental mode in the axial and transverse directions. The analytical results such as reflection coefficient *R* derived here are found to be applicable to other modes and various shapes of cavity with appropriate corrections. The present model of one-port cavity is directly applicable to our experiment carried out in a two-port cavity [23], if input and output coupling constants are the same.

The axial length l is nearly equal to one half of waveguide wavelength in the cavity. Planes 1, 2 and 3 mean, respectively, the planes of detuned short. The planes 1 and 2 coincide with the end wall of the cavity, when the coupling constant h between the cavity and the input cable tends to zero. Notation h is a given dimensionless constant of the coupling antenna, and we assume that $h^2 \ll 1$, since we consider a high Q cavity. Notation α is a round-trip attenuation at the wall of the cavity or amplification that means a production of rf energy by the CRM instability or the CIAD, and $\theta \simeq \pi/2$ is phase shift between the planes 2 and 3 in Fig. 19. We assume that $|\alpha| \ll 1$ for the high Q cavity.

From the equations (4), one obtains the reflection coefficient R of the one-port cavity as,

$$R = b_1 / a_1 = -\sqrt{1-h^2} + \frac{h^2 e^{-(\alpha+j2\theta)}}{1-\sqrt{1-h^2}\,e^{-(\alpha+j2\theta)}}. \tag{5}$$

Assuming $h^2 \ll 1$ and $|\alpha| \ll 1$, Taylor expansions are executed, and (5) is simplified to,

$$R \simeq -1 + \frac{h^2}{h^2/2 + \alpha + j2\pi G \dfrac{\Delta\omega}{\omega_0}}, \quad G = \left[1 - \left(\frac{\lambda_0'}{\lambda_c}\right)^2\right]^{-1}, \tag{6}$$

where $\Delta\omega = \omega - \omega_0$, and λ_0' and λ_c are, respectively, the free space wavelength and cutoff waveguide wavelength for a microwave frequency ω near the resonant frequency ω_0 of the cavity. The factor *G* means the difference of waveguide wavelength from that in free space, and in our designed cavity $G \simeq 25$. We introduce three Q factors as follows,

Unloaded Q factor $Q_u = \pi G / \alpha$ (7)

External Q factor $Q_e = 2\pi G / h^2$ (8)

Loaded Q factor $Q_0 = \left(\dfrac{1}{Q_u} + \dfrac{1}{Q_e}\right)^{-1} = \dfrac{Q_u Q_e}{Q_u + Q_e}$, (9)

Using (7)-(9), (6) is rewritten as,

$$R = -1 + \frac{2Q_0}{Q_e} \frac{1}{1 + j\dfrac{\omega - \omega_0}{B_0}}, B_0 = \frac{\omega_0}{2Q_0}, \tag{10}$$

where B_0 is the half half-width of the resonant curve of the cavity. The coupling factor *s* is defined as,

$$s = \frac{Q_u}{Q_e} = \frac{h^2}{2\alpha}. \tag{11}$$

It is noted that the coupling factor s defined in (11) includes the effect of beam inside the cavity and can be positive and negative values, whereas the coupling constant h defined in Fig. 19 is a positive constant of empty cavity.

Using (10), the squared reflection coefficient $|R|^2$ versus frequency to be measured by a crystal detector is calculated for various values of the coupling factor *s* in Fig. 20, where Q_e=6000 and $\omega_0/2\pi = 3.45$ GHz have been assumed. The region of positive absorption $0 < |R|^2 < 1$

corresponds to s>0, $\alpha > 0$ and Q_u>0. The loss in the cavity including beam-plasma is positive. On the other hand, the region of negative absorption $1<|R|^2$ corresponds to s<0, $\alpha < 0$ and Q_u<0. The amplification of the microwave surpasses the losses at the metal wall and in cold plasma in the cavity.

Negative absorption will be verified, if the value of $|R_{max}|^2>1$ is observed, where R_{max} is the maximum value of the reflection coefficient at the resonance $\omega = \omega_0$. However, the decreased positive absorption $0<|R_{max}|^2<1$ can be another way of verification of the CIAD in our experiment, in which a decrease in $|R_{max}|^2$ from the value without beam is observed, when spiraling electron beam is incident, if $0 < s < 1$, as in Fig. 18.

From (10) and (11), R_{max} is given by $R_{max}=(s-1)/(s+1)$. In Fig. 21, R_{max} versus the coupling factor s is plotted. Notation CC at s=1 means the critical coupling, $|R|^2=0$, of the cavity, namely, no signal of reflection b_1 in Fig. 19 is present at $\omega = \omega_0$ as shown in (10). The reflection at the plane of detuned short 1-1' and backward radiation from the cavity cancel out each other, since their amplitudes are equal and their phases are $180°$ out of phase.

Cavity without incident beam has always a positive value of s. The regions $0<s<1$ and $1<s$ are, respectively, under-coupling and over-coupling regions. NC at s=0 and $s = \pm\infty$ mean that no coupling between the input cable and the cavity is present, namely, h=0. NL at s=-1 means that infinitely large values of reflected signal is expected for an infinitely small value of input signal. Namely, self oscillation arises without input microwave on the cavity. Here, loaded Q-value, Q_0, and the time constant $\tau = 2Q_0 / \omega_0$ become infinity. The cavity is ideally superconducting and injected microwave power is accumulated unlimitedly theoretically.

Correspondence between Figs 20 and 21 is explained as follows: Four white circles in Fig. 21 are values of s shown by the curves in Fig. 20. The border line $|R|^2=1$ between positive and negative absorptions is not s=0, but $s = \pm\infty$ in Fig. 21 experimentally. If amplification by spiraling beam arises in the cavity, $s = h^2 / 2\alpha$ given by (11) increases because of decrease in α. At $s = \pm\infty$ in Fig. 21, one obtains $|R_{max}|^2=1$ that means no coupling between the cavity and the external circuit, namely h=0, in Fig. 19 and this is the border line between positive and negative absorptions.

The region s<-1 means low Q_e case in which gyrotrons with end reflections are operated. It is the purpose of our experiment to observe reflected signal $|R_{max}|^2>1$ for $s \ll -1$ in Figs 20 and 21 that is the direct evidence of negative absorption of the CIAD or the CRM instability by gyrating beam in the cavity.

When s<0 as in the cases of s=-10, -3 and -0.2 in Fig. 20, we will observe $|R_{max}|^2>1$. The observation $|R_{max}|^2>1$ at $\omega < \tilde{\Omega}$ in a case of $\omega_b^2 \gg \tilde{\Omega}^2$ is the purpose of this experimental program to detect the CIAD. An experimental demonstration of the expected signals of the negative absorption in the cavity will be shown afterward in Fig. 25.

3.2.3 Signals required for detecting negative absorption due to CIAD

Fabricated cylindrical stainless-steel cavity works at TE_{011} mode with resonant frequency 3.5 GHz. Its sizes are inner radius a=0.05415 m and variable length l=0.17-0.21 m with adjustable shorting circular disk.

Figure 22 shows the calculated curves of positive and negative absorptions as a function of axial magnetic field B_0. Here, the frequency of incident microwave is adjusted to 3.5 GHz at the resonance in empty cavity to observe the minimum $|R_{max}|^2$. The vertical axis $|R|^2$ is assumed to be proportional to attenuation constant α defined in Fig. 19 as, [3, 4, 21],

$$\alpha = \frac{\pi G}{Q_e}\left(1+\frac{2py}{1+y^2}\right), y = \frac{\omega-\omega_1}{2B_1}, \quad (12)$$

where ω_1, B_1 and p are given numerical constants to fit the positive and negative absorptions. In Fig. 22, coupling factor *s*=0.15 and other parameters shown in the figure are assumed. The given numerical parameters are somewhat different from real experimental values. Negative absorption arises for $|p|>1$ [3]. The resonant curve of the CRM instability for *p*=1.5 is depicted by solid curve, whereas the case of the CIAD for *p*=-1.5 is shown by dashed curve.

Negative absorption of the CRM instability and the CIAD could be observed, respectively, for $\omega > \tilde{\Omega}$ and $\omega < \tilde{\Omega}$ as shown in Fig. 22. In other words, the CRM and the CIAD are expected for low-field and high-field sides of $\omega = \tilde{\Omega}$ that corresponds to the axial magnetic field $B_0 = 0.3106$ T for our 15 keV beam. According as beam current increases, the region of the negative absorption is expected to move from left-hand side (solid curve) to right-hand side (dashed curve) of $B_0 = 0.1306$ T. Or, probably we may observe both negative absorptions at the same time for the incidence of high density beam such as $n \geq 1.5\times10^{11}$ cm^{-3}, where $n = 1.5\times10^{11}$ cm^{-3} corresponds to $\omega = \tilde{\Omega} = \omega_b$.

The physical meaning of $|p|>1.0$ for negative absorption is physically analogous to $N(V_\theta/c)^2 > 1$ that many gyrations in the cavity are required for detecting the resonant curves correctly, where $N \gg 1$ is number of gyrations in the cavity. The transit time of spiraling electrons is analogous to the momentum transfer collision time ν_c^{-1} in rf oscillation of the electrons in discharge plasmas. Unless the collision time is sufficiently longer than the time of gyration, namely $\tilde{\Omega} \gg \nu_c$, no cyclotron resonance can be observed [4, 20].

3.2.4 Fabricated cavity and microwave circuits for plasma-loaded CRM

The TPD-II Machine in NIFS [12, 13] has been a facility for testing the characteristics of various materials for diverters in fusion reactors with magnetic confinement. Schematic view of the TPD-II Machine and constructed plasma-loaded CRM is shown in Fig. 1. In (a), total view of the apparatus is depicted. Plasma is produced by dc helium gas discharge between a hot cathode made of LaB_6 and grounded anode of TPD-II at the right-side. Plasma is spouted out from an orifice in the anode into left-side plasma container made of quartz pipe with inner diameter 0.14 m surrounded by solenoid coils where the plasma loaded CRM is installed. This portion is evacuated by two 10 inch high speed turbo-molecular pumps to remove neutral gases for attaining fully ionized plasma. The plasma column has density up to 10^{14} cm^{-3}, temperature of a few eV and beam diameter 10 mm.

Exactly speaking, the plasma-loaded CRM consists of three different portions: (1) A pair of stainless steel mesh electrodes to apply high voltage of -15 kV for obtaining beam plasma, followed by three metal disks with pin hole to limit the beam diameter less than 10 mm, (2) a pair of helical windings of wiggler to create transverse velocity in the beam, and (3) the cylindrical cavity of TE_{011} mode to detect negative absorption of incident cw microwave near 3.45 GHz.

The principle of our plasma-loaded CRM is shown in Fig. 1(b). Beam of 15 keV with $V_\theta \simeq 0$ from TPD-II is incident into the wiggler from right-hand side. Here, the beam gets a pitch factor $\alpha \simeq 0.65$. The wiggler and the cavity are located, respectively, in the axial magnetic field of $B_s = 0.03268$ T and $B_0 = 0.1268$ T. The mirror ratio between both of them is 3.88 and the beam obtains increased pitch factor α above unity. The cavity region is immersed in a uniform axial magnetic field created by a pair of iron plates with thickness 20 mm. In Fig. 1(c), the calculated distribution of axial magnetic field in the portion of the plasma-loaded CRM is shown. The locations of 16 coils are adjusted, try and errors, so that they give the uniform fields within 3 % spatial non-uniformity. The coil currents for both fields are 72.3 A and 240 A, respectively. We

adjust the values of B_s and B_0 to attain the best performance of the plasma-loaded CRM.

Each of 16 coils consists of 30 turns water-cooled hollow conductors with cross section 1.4×1.4 mm^2. The sizes of a coil are inner and outer diameters of 21 cm and 65 cm, respectively, and the thickness is 3.5 cm. The magnetic field on the axis is calculated by Biot-Savart's law, where the hollow conductor is approximated by line current with infinitesimal cross section at the center of the conductor.

Picture of fabricated plasma-loaded CRM is shown in Fig. 23. In (a), cylindrical TE_{011} cavity made of stainless steel with movable disk inside is shown. Inner diameter of the cavity is 0.1083 m, and the length is varied from 0.17 to 0.21 m by the adjustable shorting disk. Two identical loop antennas with magnetic coupling are inserted into the side wall of the cavity, one is to feed microwave and the other is to detect the transmitted signal. The beam enters into a hole of diameter 15 mm on the axis and goes toward end target downstream, although it is not shown.

In Fig. 23(b), a pair of mesh electrodes to apply dc -15 kV high-voltage (left) and a loop antenna (right) to insert into the cavity are shown. After the pair of mesh electrodes, three stainless steel plate disks with pin hole are installed to discriminate the beam diameter less than 10 mm. The diameter of the pin hole must be adjusted, try and errors, to have the optimum signal of negative absorption due to gyrating electrons without changing appreciably the resonant frequency of the cavity as shown in Fig. 22.

Diagram of constructed microwave interferometer including the TE_{011} plasma cavity is shown in Fig. 24. We use semi-rigid cables to compose the interferometer circuits. Two-port cavity is used instead of one-port cavity analyzed in the previous sub-section **3.2.2**. The two-port cavity analyzed in [23] is identical to the one-port cavity shown in Fig. 19, if the two coupling constants are the same. The frequency of the microwave from Gunn oscillator (50 mW) is swept by an amount of 0.3 % without changing the power level. Since the cavity has loaded Q value Q_0 larger than 6000, the properties of other components in the microwave circuit do not change appreciably within the range of frequency modulation. We will change the axial magnetic field B_0 in Fig. 22 at the cavity as was done in [4]. An advantage to use two-port cavity is that we can insert microwave amplifier (AMP) up to 40 dB, Model-APA0204 (ALC microwave Ltd.) for 2-4 GHz that enables us to change incident power to the cavity from 10^{-5} to 1 W.

In near future, the measurements of negative absorption caused by the CRM instability and the CIAD will be conducted for both regions $s>1$ and $s<0$.

Transmitted signal $|T|^2$ to observe instability in the cavity is simulated by the AMP after the cavity. In Fig. 25, the maser action is demonstrated that is to compare with calculated ones in Fig. 20. The positive direction of the traces on the oscilloscope is downward, because the detector HP432B with negative polarity is used. The zero level of the transmission and reflection coefficients, $|R|^2$ and $|T|^2$ are at the top of the traces. In Fig. 25(a) and (b), the transmission signal $|T|^2$ through the empty cavity is demonstrated as positive and negative absorptions, respectively. In (a), positive absorption is obtained, when the gain of AMP in Fig. 24 is small, 0 dB. In (b), on the other hand, negative absorption is simulated, when the gain of AMP in Fig. 24 is large, 7.5 dB. Simulated negative absorption to compare with Fig. 20 is demonstrated, since equivalently rf power is created inside the cavity at resonant frequency 3.454 GHz.

The designed parameters and evaluated errors in the respective portion of the apparatus of the plasma-loaded CRM are listed in the Table 1 in page 45.

4. Discussion and Conclusion

For the first time in literature, we analyze a dispersion relation including two mechanisms of cyclotron emission from finite thickness annular beam where some electrons are free and the others are constrained in motions of gyration. The unphysical unstable modes at infinite values of axial wavenumber in slow wave region in conventional dispersion relations of the CRM instability bothered researchers for many decades are replaced by stable physical modes near the fast cyclotron

mode in our exact analysis shown in Fig. 5.

The CIAD and the CRM instability in Fig. 5 are probably coexisting mechanisms of cyclotron emission from various gyro-devices and from astrophysical plasmas.

Shefer and Bekefi measured the frequency of cyclotron emission from IREBs in uniform and rippled magnetic fields [24]. They concluded that the dominant emission was not due to collective free electron laser instability but due to the CRM instability at $\omega \simeq \tilde{\Omega}$. For low frequencies less than 10 GHz, however, only two points were shown in their Fig. 6 in which observed ω versus $\tilde{\Omega}$ were plotted. We imagine that these two data might be CIAD with $\omega < \tilde{\Omega}$ for $\omega_b^2 \gg \tilde{\Omega}^2$.

Currently, it may not be a fashionable subject of research to discuss which oscillation frequency $\omega > \tilde{\Omega}$ or $\omega < \tilde{\Omega}$ is observed in real gyrotrons. This is partly because ω is almost a fixed quantity given by the sizes of a cavity. Moreover, the distinction between $\omega > \tilde{\Omega}$ and $\omega < \tilde{\Omega}$ is practically difficult from experimental point of view, because $\tilde{\Omega}$ is a quantity spatially non-uniform, whereas ω can be measured very precisely. Note that difference between ω and $\tilde{\Omega}$ can be observed, only when a device to fit the particular purpose were carefully designed [4].

Furthermore, questions may arise: "Why is the author of this report interested in the detailed distinction between the CRM instability and the CIAD that has practically little influence on the performance of the gyrotrons?" "Do gyrotrons stop to work, if the authors' new theory is correct?" However, it should be emphasized that, sometimes, physics requires a stringent accuracy for better understandings, even though such accuracy may not be required from engineering point of view.

The CRM instability ($\omega > \tilde{\Omega}$) may not be the exclusive principle of gyrotron oscillation, because there has been no experimental verification to be $\omega > \tilde{\Omega}$ in gyrotrons. It is quite important to distinguish between $\omega > \tilde{\Omega}$ and $\omega < \tilde{\Omega}$ in cyclotron emissions in plasma physics and in gyrotron research, since physical reasons are different.

I would emphasize that the gyrotron community over the world is partly spoiled by the defect of unphysical solutions as shown in Fig. 2. We regret that fundamental understandings of physics of gyrotrons are not very firm yet, although there exist huge amount of research reports for technical and hardware developments.

No linear dispersion relation of CRM instability has been reported that the finite Larmor radius effect of gyrating relativistic electrons at the beam-vacuum interface is correctly analyzed. Our relations described in **2.2** and **2.3** are exceptions that have overcome the difficulty in a case of LO electron beams for the first time in physics of gyrotrons.

The relativistic Vlasov-Maxwell equations dealing with many electrons with different velocities that the previous researchers [5, 6] founded to analyze the CRM instability will not be Lorentz invariant. Generally speaking, electro-dynamic phenomena of relativistic electrons predicted by these equations have not been confirmed by any experimental data quantitatively for decades.

In conclusion, we have designed and fabricated a microwave interferometer circuit to detect the CIAD in addition to conventional CRM instability in plasma-loaded cylindrical cavity at 3.45 GHz. With increase in beam density, the CRM instability may be suppressed and the CIAD may take turn. In other words, frequency of negative absorption in the plasma-loaded cavity may change from above to below the relativistic electron cyclotron frequency with increase in the beam density such that $n \geq 1.5 \times 10^{11}$ cm^{-3}. Or, we may observe both negative absorptions at the same time for high density beam, because both free and constrained electrons may be present. To attain the purpose, a wiggler consisting of bifilar helical windings to create a spiraling beam in the TPD-II Machine with energy 15 keV and pitch factor $V_\theta / V_z \simeq 1.28$ has been designed.

The constrained gyration model and the resultant CIAD described in this report remains only a proposal at this moment, until the physical existence is verified experimentally. In this experimental program, we try to observe the new principle of cyclotron emission different from the CRM instability. The present experimental study contributes to a deeper understanding and a widened future prospect in gyrotron research.

Appendix A: The physical reason of constrained gyration model.

Traditionally, cyclotron emission has been analyzed under the assumption that beam electrons are tenuous enough to neglect the effects of neutralizing ions [24]. This conventional assumption is named "free gyration model" in this report. Previous researchers [3-8] of CRM instability have followed this model applicable for tenuous beams such as $\omega_b^2 \ll \tilde{\Omega}^2$.

Moreover, there can exist an extended free gyration model for cyclotron emission where the free gyration of mobile electrons is always possible in the presence or absence of uniform immobile ions, regardless of the ion density. Free gyration may be allowed even in high density neutralized electron beams.

On the other hand, there can be another extreme model for the electron gyration. In some occasions, free gyration may be prevented by a restoring force caused by the charge separation between dislocated electrons and localized immobile ions, if $\omega_b^2 \gg \tilde{\Omega}^2$. We assume that the localized ions are cold and their Larmor radii are much smaller than that of the energetic electrons. This model adopted in this report is called "constrained gyration model."

The free gyration model applicable for $\omega_b^2 \ll \tilde{\Omega}^2$ results in the conventional understanding that the CRM instability is the unique principle of cyclotron emission from the electrons.

On the other hand, the constrained gyration model for $\omega_b^2 \gg \tilde{\Omega}^2$ yields prediction that the CIAD can be another principle of cyclotron emission in addition to the CRM instability. How adequate are the both models in practical physical situations realized experimentally has not been clarified thoroughly yet and is left as an open question. The constrained gyration model which prohibits radial displacement of electrons in infinitely thin annular beam may be somewhat too strange for the readers to trust as a real physical situation. Here, we clarify the reason why the constrained gyration model can be a logical existence.

We consider a cylindrical waveguide with radius r_{cav} shown in Fig. 3, including infinitely thin thickness mono-energetic LO electron beam with radius r_b. The beam is guided by a uniform axial magnetic field of strength $\boldsymbol{B}_0 = (0,0,B_0)$ and ion background is assumed to entirely neutralize static space charge electric field in the beam. In equilibrium state, an electron fluid element has velocity $\boldsymbol{V}_0 = (0,V_\theta,V_z)$, where the guiding centers are assumed to lie on the center axis of the waveguide. Relativistic factor γ_0 can be expressed as $\gamma_0 = \left(1-\boldsymbol{V}_0\cdot\boldsymbol{V}_0/c^2\right)^{-1/2}$. We assume $\partial\gamma_0/\partial r = 0$ for brevity.

A spatial and temporal perturbation in the fluid element in the form $\exp\left[-i\left(\omega t - k_z z - l\theta\right)\right]$ is assumed, where *l* is azimuthal mode number. First order perturbations in velocity, induced rf electric and magnetic fields are denoted, respectively as, $\boldsymbol{v} = (v_r,v_\theta,v_z)$, $\boldsymbol{E} = (E_r,E_\theta,E_z)$ and $\boldsymbol{B} = (B_r,B_\theta,B_z)$. Their practical forms are listed in [9] by solving a system of fluid equation of motion, equation of continuity and Maxwell equations. The first order perturbation in relativistic factor γ_1 is expressed as $\gamma_1 = \left(V_\theta v_\theta + V_z v_z\right)\gamma_0^{\,3}/c^2$. Surface charge density in unperturbed state is denoted as $\sigma_0 = -en_0\varepsilon$, where the beam thickness ε tends to zero. Quantities enclosed by brackets $\langle\ \rangle$ signify their value at the center of the thin beam thickness ε. For an infinitely thin thickness, $\left\langle \frac{dE_\theta}{dr} \right\rangle$ and $\left\langle \frac{dE_z}{dr} \right\rangle$ vanish because E_θ and E_z are continuous across the beam thickness. The value of $\langle E_r \rangle$ is originally undetermined.

The perturbed current density, $\boldsymbol{j}_r = -e\left(n_0\boldsymbol{v} + n_1\boldsymbol{V}_0\right)$, is integrated across the beam thickness ε

to give the following expression for the surface current density $\boldsymbol{\kappa}$:

$$\boldsymbol{\kappa} = \sigma_1 \left(\tilde{\Omega} r_b \hat{e}_\theta + V_z \hat{e}_z \right) - \lim_{\varepsilon \to 0} \frac{e}{r_b} \int_{r_b - \varepsilon/2}^{r_b + \varepsilon/2} n_0 \boldsymbol{v} r dr \tag{A 1}$$

$$\begin{bmatrix} \kappa_\theta \\ \kappa_z \end{bmatrix} = \frac{e\sigma_0}{\gamma_0 m} \begin{bmatrix} s_{22} & s_{23} \\ s_{32} & s_{33} \end{bmatrix} \begin{bmatrix} E_\theta \\ E_z \end{bmatrix} \tag{A 2}$$

$$\begin{aligned} s_{22} &= i \left\{ -(\omega - k_z V_z)^2 + \tilde{\Omega}^2 r_b^2 \beta^2 \right\} / \omega_l^2 \omega, \\ s_{23} = s_{32} &= i \left[\left\{ -l V_z (\omega - k_z V_z) / r_b + V_z r_b \tilde{\Omega} \omega^2 / c^2 - \tilde{\Omega} r_b k_z (\omega - l\tilde{\Omega}) \right\} \right] / \omega_l^2 \omega, \\ s_{33} &= i \left\{ (\omega^2 / c^2 - l^2 / r_b^2) V_z^2 - (\omega - l\tilde{\Omega})^2 \right\} / \omega_l^2 \omega. \end{aligned} \tag{A 3}$$

Here, $\omega_l = \omega - V_z k_z - l\tilde{\Omega}$, σ_1 is the first order surface charge density at $r = r_b$ derived in [9]. We have taken a limit of the thickness $\varepsilon \to 0$ that was not executed in the previous analyses [7, 8]. In this limit, the radial component of (A 1) is proved to be zero as follows. The radial component of the Maxwell equation, $\nabla \times \vec{B} + i\omega \vec{E} / c^2 = \mu_0 \vec{j}_1$, is expressed as,

$$\frac{il}{r} B_z - i k_z B_\theta + \frac{i\omega}{c^2} E_r = \mu_0 j_r \tag{A 4}$$

where, μ_0 is the permeability in vacuum. Multiplying rdr to (A 4) and integration across the beam thickness is made. Here, E_r, B_θ and B_z at $r = r_b$ are discontinuous and unknown yet at this moment. However, they have anyway finite values inside the beam thickness ε from $r = r_b - \varepsilon/2$ to $r = r_b + \varepsilon/2$. Each term at left-hand side after the integration is zero in the limit of $\varepsilon \to 0$, and the following expression is derived as,

$$\kappa_r = \frac{1}{r_b} \int_{r_b - \varepsilon/2}^{r_b + \varepsilon/2} j_r r dr = 0 . \tag{A 5}$$

Accordingly, one obtains from eq. (1) in [9],

$$\left\langle E_r \right\rangle = -i \frac{l\tilde{\Omega}}{\omega_l^2 r_b} \left(\tilde{\Omega} r_b E_\theta + V_z E_z \right), \tag{A 6}$$

$$v_r = -\frac{ie\omega_l^2}{\gamma_0 m \left(\omega_l^2 - \omega_1^2 \right) \omega} \left[E_r - \left\langle E_r \right\rangle \right] = 0 , \tag{A 7}$$

confirming that the motion of electron fluid is constrained in radial direction. The electrons must stay on the original LO at any moment. This model of constrained gyration is quite different from the previous analyses [3-8], where non-zero rf velocity in the radial direction was assumed beforehand. In other words, the electrons can dislocate from the LO in their free gyration model that results in CRM instability. Note that the annular beam cannot be infinitely thin thickness, if the radial excursion of the electrons is allowed.

Constrained gyrations happen in case of infinitely thin thickness high-density annular beam neutralized by localized cold ions [9]. In such case, the CRM instability is suppressed, and another instability for cyclotron emission, namely the CIAD, arises. One needs to assume a non-zero thickness $\varepsilon \neq 0$ to have a quantitative relationship of the CRM instability taking into account the finite Larmor radius effect at the beam-vacuum interface.

Appendix B: Derivation of an exact dispersion relation for infinitely thin thickness annular beam (Fig. 4)

The derivation of our exact linear dispersion relation for infinitely thin-thickness beam in the cylindrical waveguide shown in Fig. 3 is here summarized. The following six boundary conditions

are chosen. The boundary conditions at $r = r_b$ of the infinitely thin-thickness beam are, $E_\theta^{II} - E_\theta^{I} = 0$, $E_z^{II} - E_z^{I} = 0$, $B_\theta^{II} - B_\theta^{I} = \mu_0 \kappa_z^-$ and $B_z^{II} - B_z^{I} = -\mu_0 \kappa_\theta^-$. The boundary conditions at the surface of cylindrical waveguide at $r = r_{cav}$ are, $E_\theta^{II} = 0$ and $E_z^{II} = 0$.

In regions I $(0 \le r \le r_b)$ and III $(r_b \le r \le r_{cav})$ in Fig. 3, the distributions of rf electric and magnetic fields in vacuum are derived for Q-TE$_{11}$ mode by solving the conventional Bessel-type differential equations. Joining these six conditions and using the expressions for surface current density given by (A 2) and (A 3), one gets the following dispersion relation of the system in a form of the 6×6 determinant that must be zero:

$$\det\begin{bmatrix} J_l(\beta r_b) & -J_l(\beta r_b) & -Y_l(\beta r_b) & 0 & 0 & 0 \\ 0 & 0 & 0 & J_l'(\beta r_b) & -J_l'(\beta r_b) & -Y_l'(\beta r_b) \\ D_{31} & \frac{i\omega}{c} J_l'(\beta r_b) & \frac{i\omega}{c} Y_l'(\beta r_b) & D_{34} & -\frac{k_z l}{\beta r_b} J_l(\beta r_b) & -\frac{k_z l}{\beta r_b} Y_l(\beta r_b) \\ D_{41} & 0 & 0 & D_{44} & \beta J_l(\beta r_b) & \beta Y_l(\beta r_b) \\ 0 & J_l(\beta R_0) & Y_l(\beta R_0) & 0 & 0 & 0 \\ 0 & 0 & 0 & 0 & J_l'(\beta R_0) & Y_l'(\beta R_0) \end{bmatrix} = 0 \qquad \text{(B 1)}$$

where,

$$D_{31} = -i(\omega/c) J_l'(\beta r_b) - cg(s_{23} l k_z / \beta r_b - s_{33}\beta) J_l(\beta r_b),$$
$$D_{34} = (l k_z / \beta r_b) J_l(\beta r_b) - i\omega g s_{23} J_l'(\beta r_b),$$
$$D_{41} = cg(s_{22} l k_z / \beta r_b - s_{23}\beta) J_l(\beta r_b),$$
$$D_{44} = i\omega g s_{22} J_l'(\beta r_b) - \beta J_l(\beta r_b).$$

Here, the azimuthal mode number $l = 1$ is chosen in numerical calculation shown in Fig, 4, and

$$g = 0.117 \, |I_b(kA)| / \beta_z r_b, \beta_z = (1 - V_z^2 / c^2)^{-1/2},$$
$$\beta = (\omega^2 / c^2 - k_z^2)^{1/2},$$
$$J_l'(\beta r_b) = (d / d\beta r) J_l(\beta r_b), Y_l'(\beta r_b) = (d / d\beta r) Y_l(\beta r_b).$$

Appendix C: Derivation of an exact dispersion relations for finite thickness annular beam (Fig. 5)

In this case, the derivation is somewhat more complicated than the previous case described in the Appendix B, because of an increase in number of boundaries from three to four in Fig. 3.

The ten boundary conditions are chosen as follows: At the inner boundary of the beam $r = r_b^-$: $E_\theta^{II} - E_\theta^{I} = 0$, $E_z^{II} - E_z^{I} = 0$, $B_\theta^{II} - B_\theta^{I} = \mu_0 \kappa_z^-$ and $B_z^{II} - B_z^{I} = -\mu_0 \kappa_\theta^-$. At the outer boundary of the beam $r = r_b^+$: $E_\theta^{III} - E_\theta^{II} = 0$, $E_z^{III} - E_z^{II} = 0$, $B_\theta^{III} - B_\theta^{II} = \mu_0 \kappa_z^+$ and $B_z^{III} - B_z^{II} = -\mu_0 \kappa_\theta^+$. At the boundary of the waveguide $r = r_{cav}$: $E_\theta^{III} = 0$ and $E_z^{III} = 0$. Here, $\kappa_2^{\pm}$ and $\kappa_3^{\pm}$ are, respectively, the surface current densities similar to (A 3) at the beam-vacuum interfaces. The above set of ten relations yields the following dispersion relation:

$$\det[D]=0, \qquad \text{(C 1)}$$

where the practical forms of the elements D_{ij}, i,j=1-10, are under submission elsewhere.

Appendix D: The equations used in the particle simulation (Figs 6-9)

The constraint is modeled by a restoring force towards the original LO circle as follows. The phenomenological potential well *U* in the radial direction for the gyrating electrons toward the original LO circle is expressed as $U = -(ne/2\varepsilon_0)(r - r_b)^2$. The resultant restoring electric field for the displacement $\Delta\vec{r} = \vec{r} - \hat{r}r_b$ of the electrons from the LO circle is given by $\vec{E} = -\partial U/\partial\vec{r} = (ne/\varepsilon_0)(\vec{r} - \hat{r}r_b)$, where $\hat{r}$ is the unit vector in the radial direction.

The following relations obtained from the relativistic equation of motion of an electron are solved numerically.

$$\frac{dv_x}{dt} = -\frac{e}{m\gamma}\left[\left(1-\frac{v_x^2}{c^2}\right)D_x - \frac{v_x v_y}{c^2}D_y + v_y B_z - v_z B_y\right],$$

$$\frac{dv_y}{dt} = -\frac{e}{m\gamma}\left[-\frac{v_x v_y}{c^2}D_x + \left(1-\frac{v_y^2}{c^2}\right)D_y + v_z B_x - v_x B_z\right],$$

$$\frac{dv_z}{dt} = -\frac{e}{m\gamma}\left[-\frac{v_z(v_x D_x + v_y D_y)}{c^2} + v_x B_y - v_y B_x\right],$$

where,

$$D_x = -E_{rf}\sin\omega t + \frac{ne}{\varepsilon_0}\left(1-\frac{r_b}{r}\right)x,$$

$$D_y = E_{rf}\cos\omega t + \frac{ne}{\varepsilon_0}\left(1-\frac{r_b}{r}\right)y, \qquad \text{(D 1)}$$

$$B_x = -\frac{\sqrt{\varepsilon_s}}{c}D_y, B_y = \frac{\sqrt{\varepsilon_s}}{c}D_x, B_z = B_0,$$

$$r_b = V_\theta/\tilde{\Omega}, r = \sqrt{x^2+y^2}.$$

Here, ε_s is specific dielectric constant within the scope of linear treatment. The first and the second terms in D_x and D_y are, respectively, the circularly polarized rf electric field and the restoring electric field due to the charge separation. Equations (D 1) are solved numerically in sub-section **2.4**. In our model, the beam current is included through the beam density *n* in the potential well with a given constant ne/ε_0 in (D 1).

Acknowledgments

This work is carried out under the collaborative research program NIFS04KQHH002, "Fundamental Experiment of Plasma-Loaded Cyclotron Maser Using TPD-II Machine," at National Institute for Fusion Science, Japan. The author would like to thank profoundly Professor Kuninori Sato, NIFS, for his thoughtful and respected supervision. Thanks are also due to Dr. Akihiro Matsubara, NIFS, for kind collaborations and stimulating discussions. The theoretical works by Dr. Yaduvendra Choyal, Devi Ahilya University, India, have motivated this experimental program. Valuable discussions and advice by Dr. Gregory Nusinovich, University of Maryland, USA, are gratefully acknowledged.

References

[1] R. J. Barker and E. Schamiloglu, *High-Power Microwave Sources and Technologies*, New York: IEEE Press, 2001.

[2] G. S. Nusinovich, *Introduction to the physics of gyrotrons*, Baltimore: Johns Hopkins Univ. Press, 2004.

[3] J. Schneider, "Stimulated emission of radiation by relativistic electrons in a magnetic field," *Phys. Rev. Lett*. vol. 2, pp. 504-505, 1959.

[4] J. L. Hirshfield and J. M. Wachtel, "Electron cyclotron maser," *Phys. Rev. Lett*. vol. 12, pp. 533-536, 1964.

[5] P. Sprangle, and A. T. Drobot, "The linear and self-consistent nonlinear theory of the electron cyclotron maser instability," *IEEE Trans. MTT*, vol. 25, pp.528-544, 1977.

[6] K. R. Chu and J. L. Hirshfield, "Comparative study of the axial and azimuthal bunching mechanisms in electromagnetic cyclotron instabilities," *Phys. Fluids*, vol. 21, pp. 461-466, 1978.

[7] Y. Y. Lau, "Simple macroscopic theory of cyclotron maser instabilities," *IEEE Trans. Electron Devices*, vol. 29, pp. 320-335, 1982.

[8] W. Lawson and C. D. Striffler, "A linear growth rate fliud formulation for large orbit, annular electron layers with finite thickness," *Phys. Fluids*, vol. 29, pp. 1682-1694, 1986.

[9] Y. Choyal, T. Watanabe and K. Minami, "Microwave excitation by a constrained large-orbit electron beam-A unified dispersion relation for slow- and fast-wave devices," *IEEE Trans Plasma Sci*. vol. 32, pp. 1298-1309, 2004.

[10] K. Minami, Y. Choyal, and T. Watanabe, "Proposal of a new principle of cyclotron emission from neutralized electron beams," *J. Plasma Phys.* vol. 73, pp. 523-541, 2007.

[11] V. L. Bratman, N. S. Ginzburg, G. S. Nusinovich, M. I. Petelin and P. S. Strelkov, "Relativistic gyrotrons and cyclotron autoresonance masers," *Int. J. Electron.*, vol. 51, pp. 541-567, 1981.

[12] K. Sato, M. Ohtsuka and M. Mimura, "Intensity calibration of VUV system by branching line pairs of low ionized light atoms," *Appl. Opt.* vol. 23, pp. 3336-3340, 1984.

[13] A. Matsubara, T. Watanabe, T. Sugimoto, S. Sudo and K. Sato, *J. Nucl. Mater.* vol. 337-339, pp. 181-185, 2005.

[14] P. M. Bellan, *Fundamentals of Plasma Physics*, New York: Cambridge Univ. Press, p. 260, 2006.

[15] Y. Choyal (private communication).

[16] D. Sarafyan, "Improved sixth-order Runge-Kutta formulas and approximate continuous solution of ordinary differential equations," *J. Math. Anal. Appl.*, vol. 40, pp. 436-445, 1972.

[17] R. C. Wingerson, "Corkscrew-A device for changing the magnetic moment of charged particles in a magnetic field," *Phys. Rev. Lett.* vol. 6, pp. 446-448, 1961.

[18] B. M. Kincaid, "A short-period wiggler as an improved source of cyclotron radiation," *J. Appl. Phys.* vol. 48, pp. 2684-2691, 1977.

[19] J. P. Blewett and R. Chasman, "Orbits and fields in the helical wiggler," *J. Appl. Phys.* vol. 48, pp. 2692-2698, 1977.

[20] J. M. Wachtel, *Ph. D. Dissertation, Yale Univ.*, p. 30-32, 1967 (unpublished).

[21] J. P. Gordon, "Variable coupling reflection cavity for microwave spectroscopy," *Rev. Sci. Instrum.* vol. 32, pp. 658-661, 1961.

[22] J. L. Altman, *Microwave Circuits*, New York: van Nostrand, p. 202, 1964.

[23] K. Minami, Y. Yamanishi, C. Kojima, M. Shindo and O. Ishihara, "Very slowly decaying afterglow plasma in cryogenic helium gas," *IEEE Trans. Plasma Sci.*, vol. 31, pp. 429-439, 2003.

[24] R. E. Shefer and G. Bekefi, "Cyclotron emission from intense relativistic electron beams in uniform and rippled magnetic fields," *Int. J. Electron.* vol. 51, pp. 569-582, 1981.

(a)

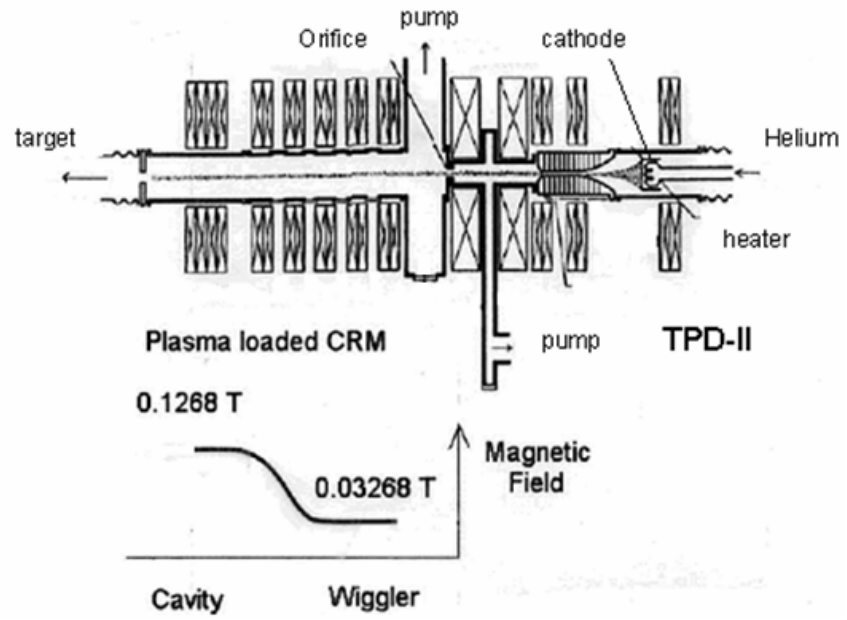

(b)

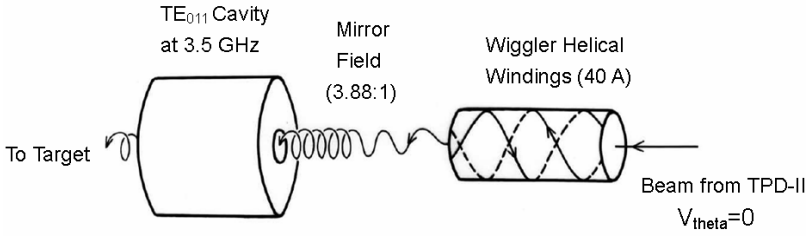

(c)

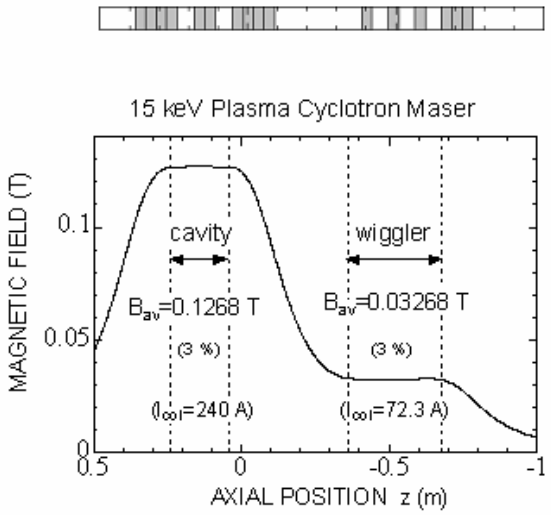

Fig. 1 Plasma-loaded CRM installed inside the TPD-II Machine, NIFS, Japan. (a) Total view. (b) Principle of operation of plasma-loaded CRM. (c) Distribution of axial magnetic field in the wiggler and the cavity. Bar code at the top shows the locations of 16 pancake coils.

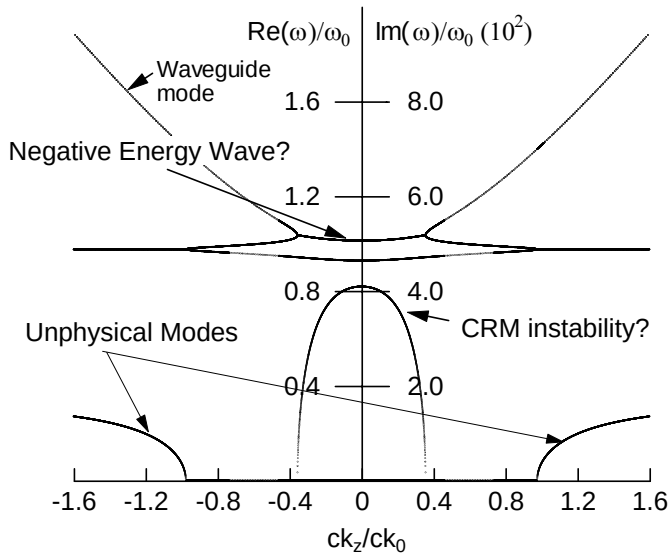

γ_{perp}=1.2, $\omega/\mathrm{sqrt}(\gamma_{perp})=0.05\ \omega_0$

$\omega_0=ck_0$, $k_0=\Omega/\mathrm{sqrt}(\gamma_{perp})$

a=1.445 cm, B=0.217 T

Fig. 2 Numerical example of conventional linear dispersion relation for CRM instability [5].

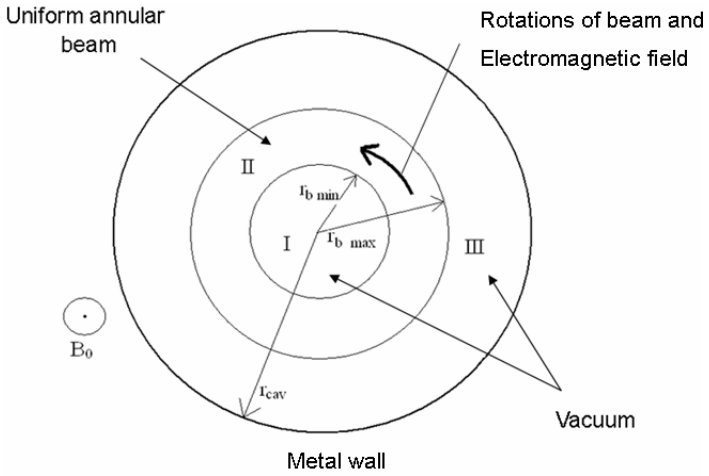

Fig. 3 Model of our exact linear dispersion relation for CRM instability and CIAD. Cross-sectional view of circular waveguide including large orbit beam in region II is shown. Regions I and III are in vacuum. Circular arrow means the counterclockwise rotations of electrons and electromagnetic field.

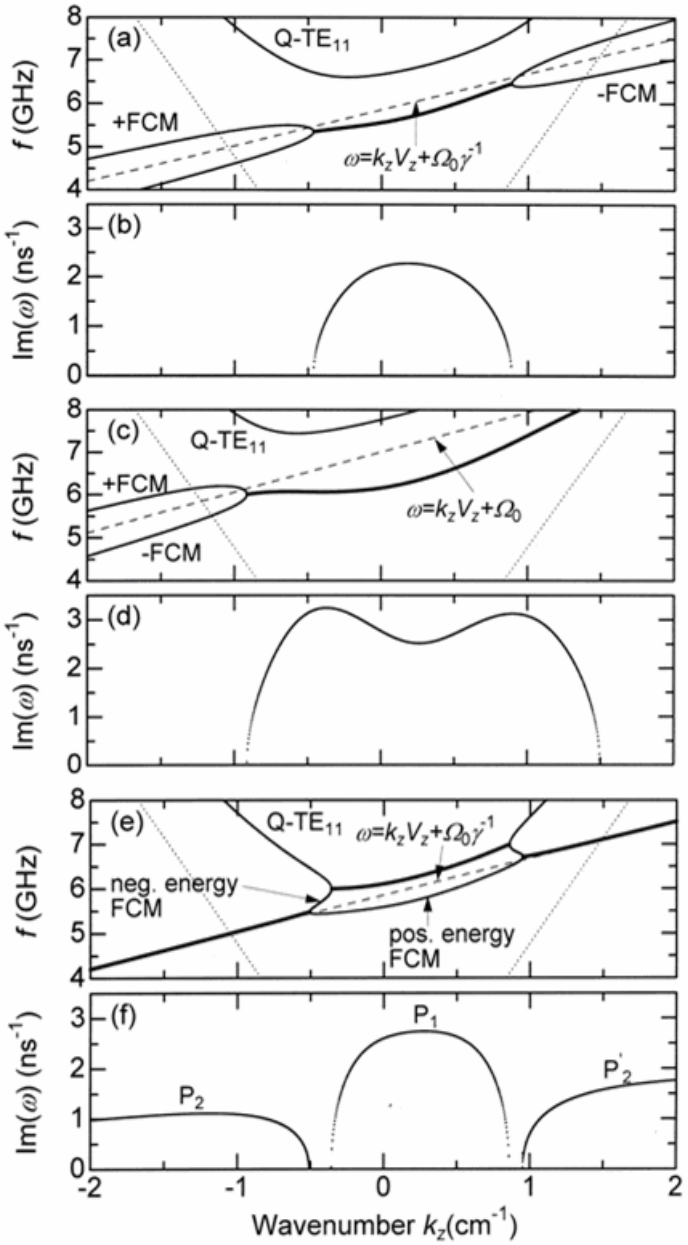

Fig. 4 Dispersion curves of CIAD (not CRM instability) for the parameters E_b=100 kV, I_b=10 A, α=3.0, B_0=0.2 T, h=0 and r_{cav}=1.445 cm [9]. In (a) and (b), all the terms are retained. In (c) and (d), only non-relativistic terms are retained by assuming $c \to \infty$, while in (e) and (f), all the non-relativistic terms are dropped without legitimacy by assuming $c \to 0$. Frequency Re(ω)/2π vs. real wavenumber k_z, are depicted in (a), (c), and (e). Corresponding temporal growth rate Im(ω) vs. real k_z is shown in (b), (d), and (f), respectively. In (a), (c) and (e), the thin dotted lines denote $f = \pm k_z c/2\pi$, while dashed lines denoted by FCM are fast cyclotron mode when space charges are ignored.

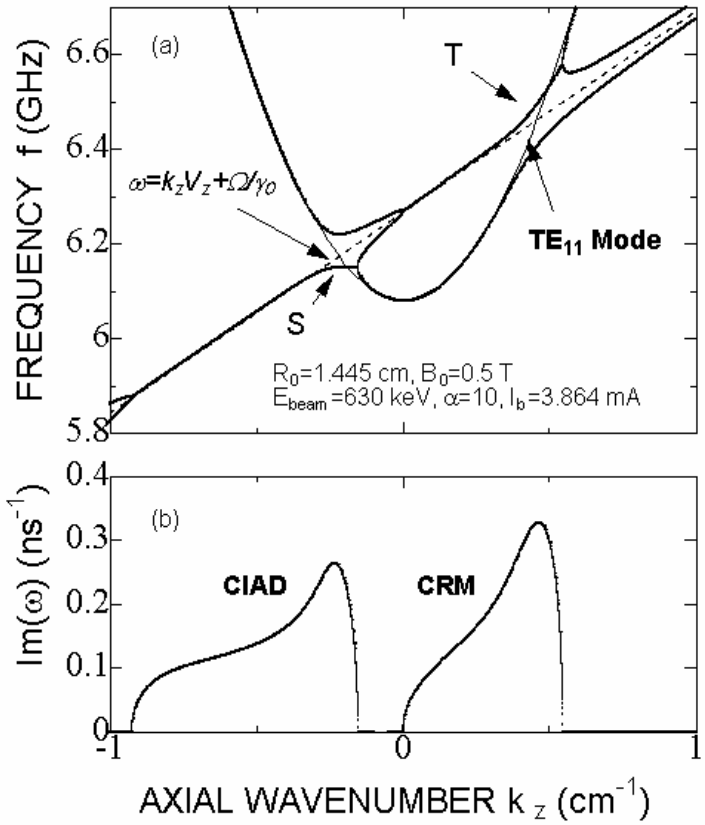

Fig. 5 Numerical example of our new linear dispersion relation (C 1) for quasi-TE_{11} mode with large orbit annular beam with finite-thickness. Given parameters are shown in the figure. (a) Oscillation frequency f (GHz) vs. k_z (cm^{-1}). Two negative energy waves, namely CIAD with $\mathrm{Re}(\omega) < \tilde{\Omega}$ and CRM instability with $\mathrm{Re}(\omega) > \tilde{\Omega}$ denoted, respectively, by S and T, are observed at the same time. (b) Temporal growth rate $\mathrm{Im}(\omega)$ (ns^{-1}) vs. k_z (cm^{-1}).

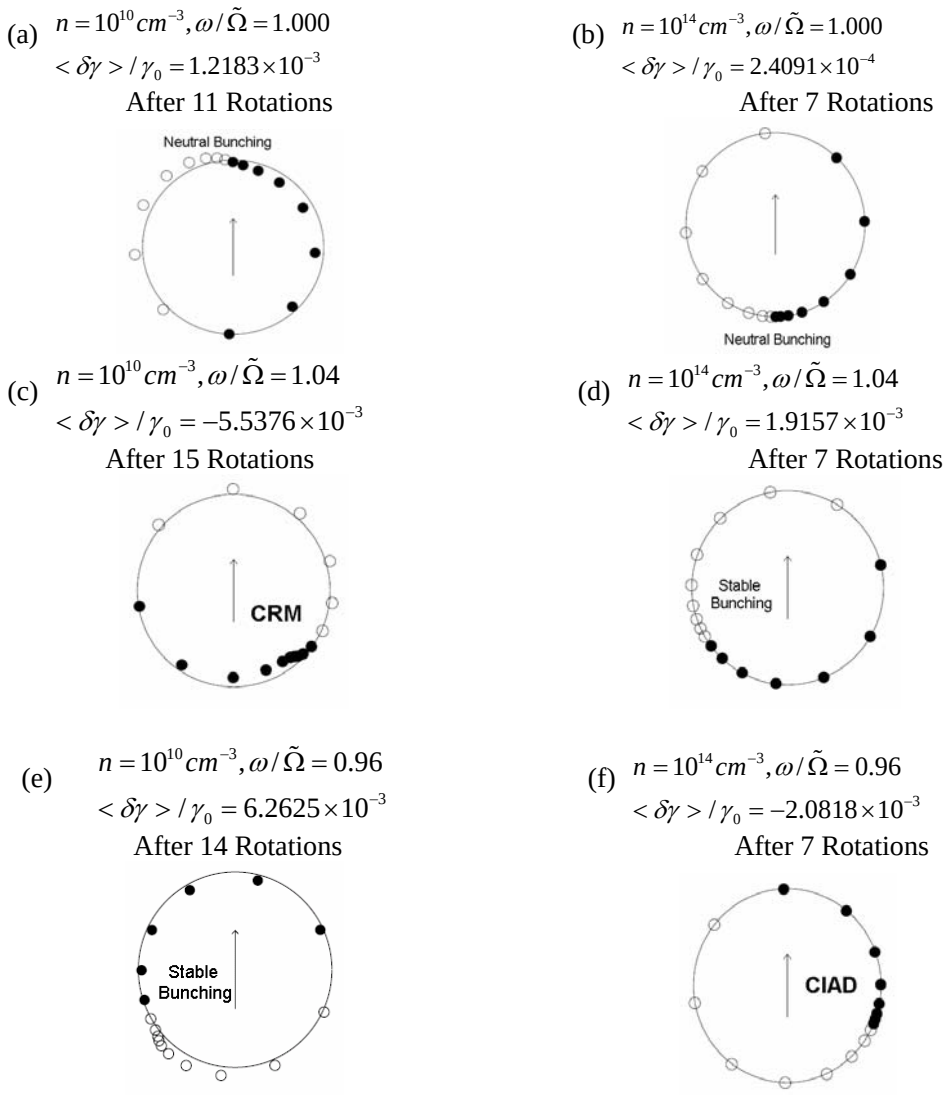

Fig. 6 Bunching of 16 test electrons after 7-15 rotations of rf field for six typical cases. Physical mechanisms of CRM instability and CIAD are clearly distinguished. The axial magnetic field B_0 =1.0 T in the direction from the sheet to our eyes, the initial pitch angle of velocity of electrons $\alpha = V_\theta / V_z = 1.0$, initial electron energy E_b=100 keV, and constant rf field amplitude $E_{rf}=3\times10^5$ V/m are assumed. Electrons and rf electric field are rotating counterclockwise. Upward arrow in each LO circle shows the direction of rf electric field at initial moment and after the rotations. Small black and white circles are, respectively, the locations of the electrons that lose and gain net kinetic energy against the rf field, respectively. We find, in (c), cyclotron resonance maser (CRM) instability and, in (f), Cherenkov instability in azimuthal direction (CIAD).

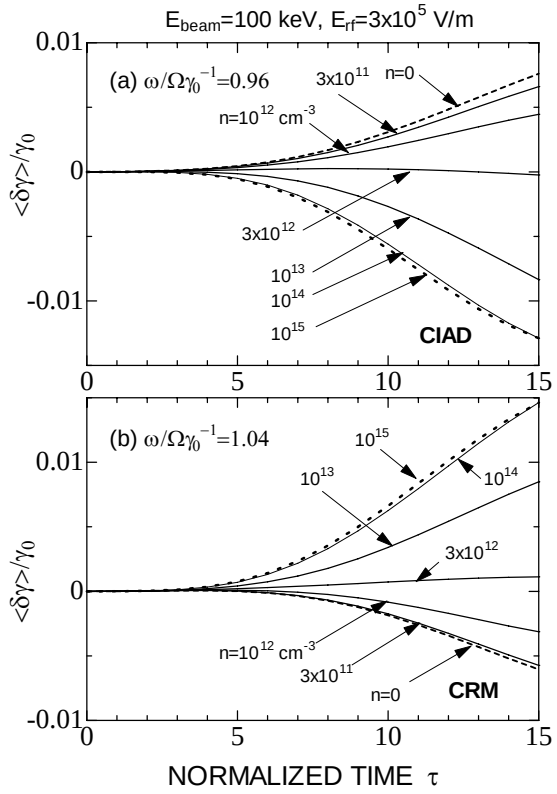

Fig. 7 Temporal changes in relative energy gain $<\delta\gamma>/\gamma_0$ up to τ =15 of gyrations for initial electron energy E_b=100 keV and E_{rf}=3×10^5 V/m. (a) $\omega/\tilde{\Omega}$ =0.96, and CIAD is observed for n>3×10^{12} cm^{-3}. (b) $\omega/\tilde{\Omega}$ =1.04, and CRM instability is observed for n<3×10^{12} cm^{-3}.

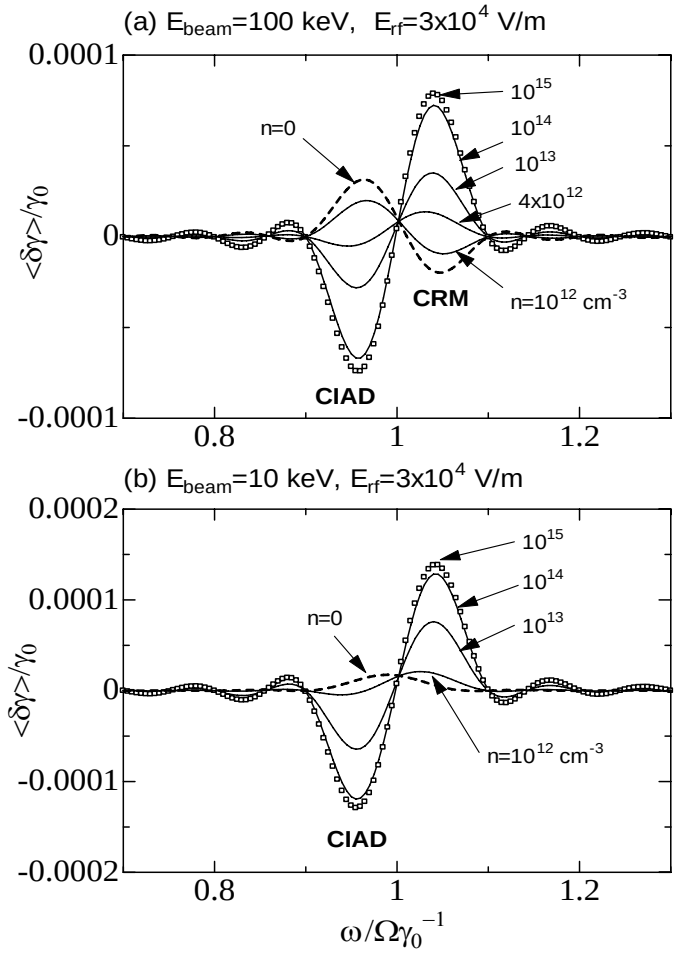

Fig. 8 Relative energy gain $<\delta\gamma>/\gamma_0$ of the 128 electrons vs. $\omega/\tilde{\Omega}$ after 10 gyrations. The constant amplitude of rf field is $E_{rf}=3\times10^4$ V/m. (a) E_b=100 keV. CIAD is observed for $n>2\times10^{12}$ cm^{-3} and for $\omega/\tilde{\Omega}<1$, on the other hand, CRM instability is found for $n<2\times10^{12}$ cm^{-3} and for $\omega/\tilde{\Omega}>1$. (b) E_b=10 keV, and CRM instability is not observed for any density n. CIAD is observed for $n>10^{12}$ cm^{-3} and for $\omega/\tilde{\Omega}<1$.

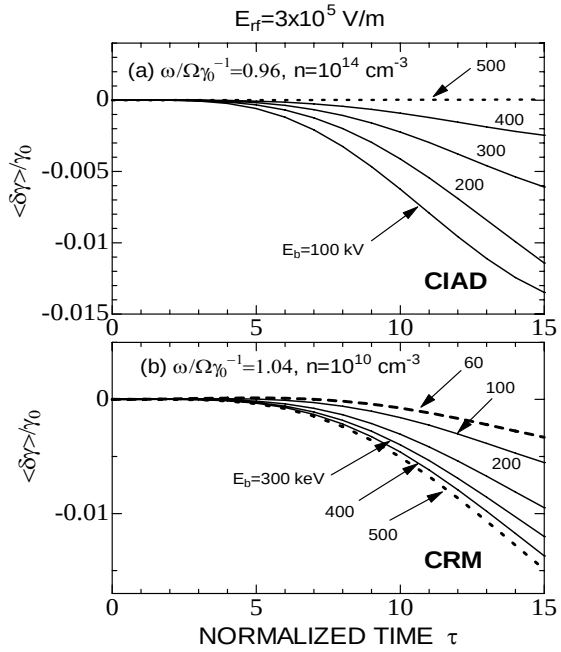

Fig. 9 Temporal changes in the relative energy gain $<\delta\gamma>/\gamma_0$ up to τ =15 of gyrations for various values of beam energy E_b. Oscillation can occur, if $\langle\delta\gamma\rangle < 0$. (a) $\omega/\tilde{\Omega}$=0.96 and $n = 10^{14}$ cm^{-3}. The CIAD is observed only for E_b<500 keV. (b) $\omega/\tilde{\Omega}$=1.04 and $n = 10^{10}$ cm^{-3}. The CRM instability is enhanced with increase in E_b.

(a)

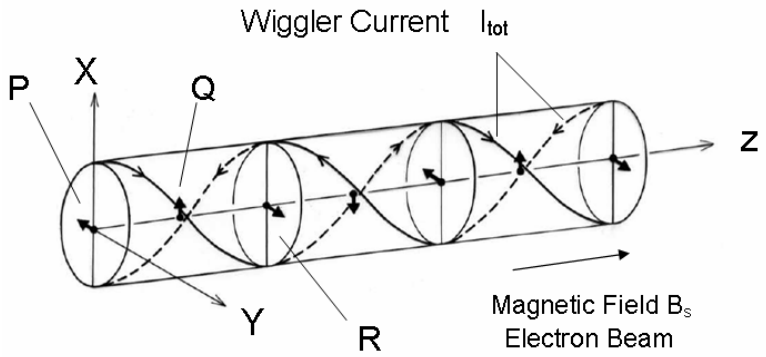

(b)

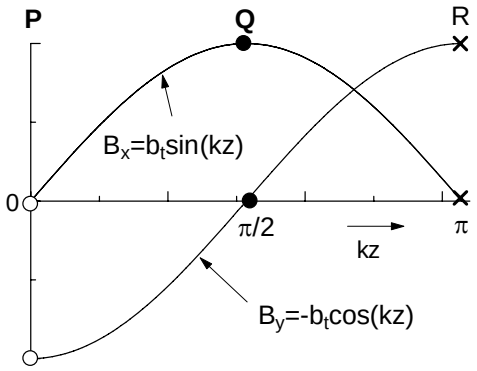

Fig. 10 Configuration of wiggler. (a) Bifilar circularly polarized helical windings and generated magnetic field b_t on the z axis. (b) Changes in helical magnetic field B_x and B_y in axial direction.

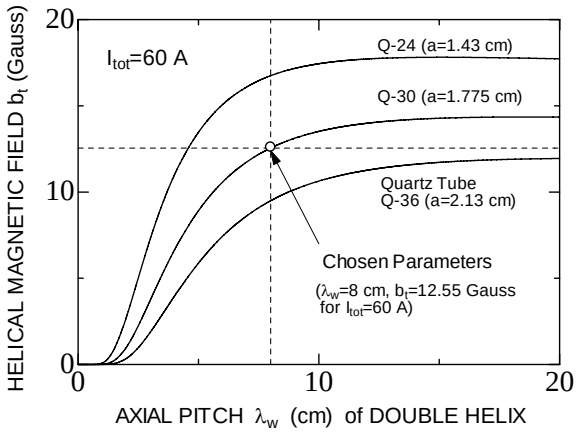

Fig. 11 Design study of axial pitch length λ_w of wiggler for creating mono-energetic spiral electron beam. White circle indicates our chosen parameters.

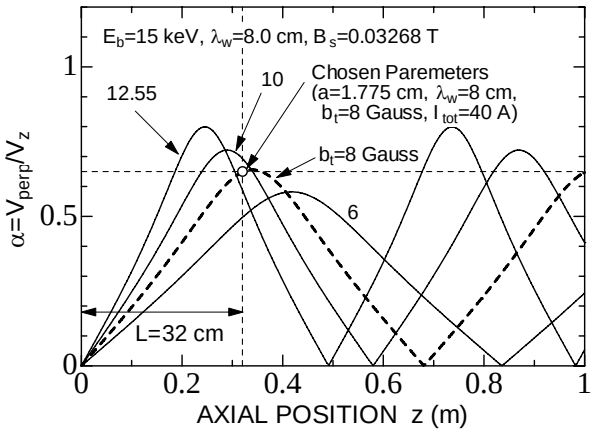

Fig. 12 Changes in $\alpha = V_\theta / V_z$ vs. axial position are calculated for various values of helical magnetic field b_t (Gauss) for beam energy E_b=15 keV, helix pitch length $\lambda_w = 8.0$ cm, B_s=0.03268 T and α (initial)=0.001. White circle is chosen parameters. Four turn helical windings with total length L=32 cm are designed.

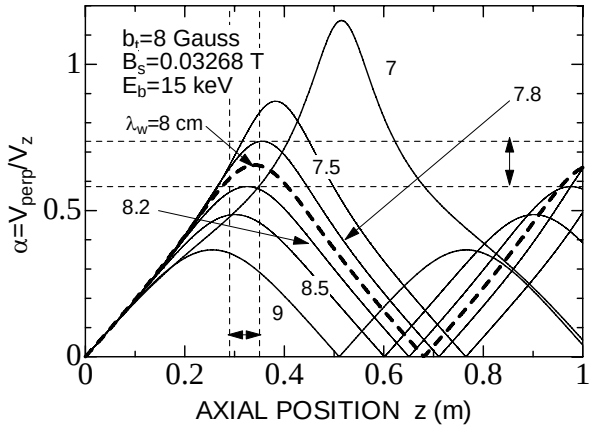

Fig. 13 Erroneous changes in $\alpha = V_\theta / V_z$ vs. axial position are calculated for various values of helical pitch length λ_w (cm) for beam energy $E_b = 15$ keV, helical magnetic field $b_t = 8$ Gauss, $B_s = 0.03268$ T and α (initial)=0.001. The dashed curve is chosen. Square made by four dashed lines is a region of expected errors in our designed parameters.

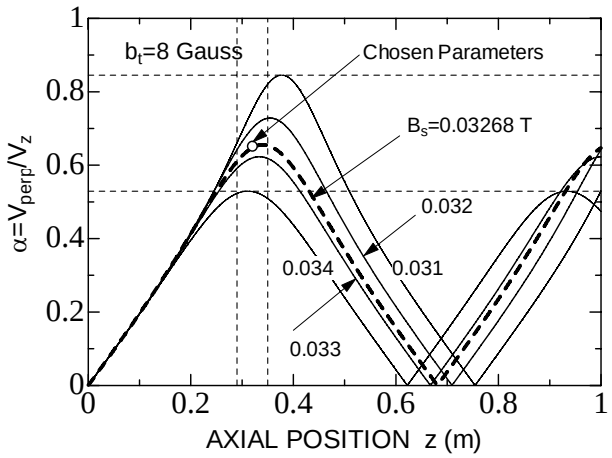

Fig. 14 Erroneous changes in $\alpha = V_\theta / V_z$ vs. axial position are calculated for various values of axial magnetic field B_s for helical magnetic field $b_t = 8$ Gauss, beam energy $E_b = 15$ keV, helical pitch length $\lambda_w = 8$ cm and α (initial)=0.001. Thick dashed curve is chosen. Square made by four dashed lines is a region of expected errors in our designed parameters.

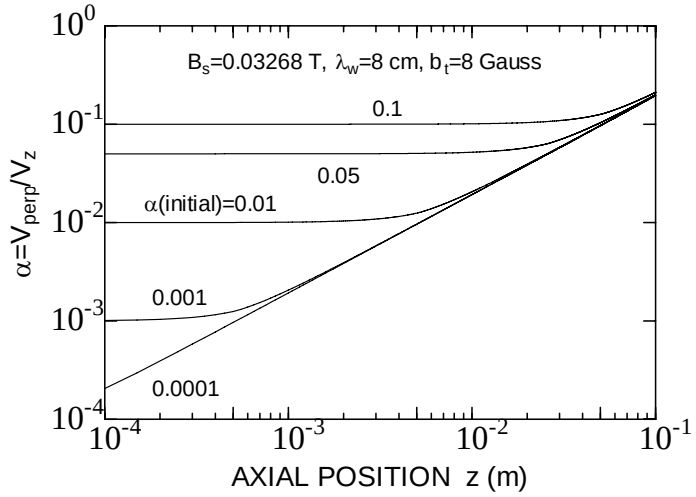

Fig. 15 Increase in $\alpha = V_\perp / V_z$ for various initial values. $E_b = 15$ keV and other parameters are given in the figure. The attained α becomes independent from the initial values after a few gyrations, if α (initial) $\ll$ 1.

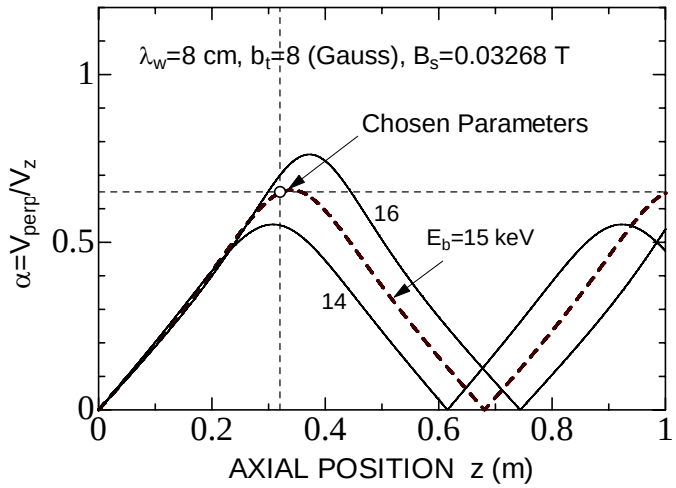

Fig. 16 Erroneous changes in $\alpha = V_\theta / V_z$ vs. axial position are calculated for three values of beam energy E_b for α (initial)=0.001. Other parameters are given in the figure. Thick dashed curve and white circle are chosen parameters.

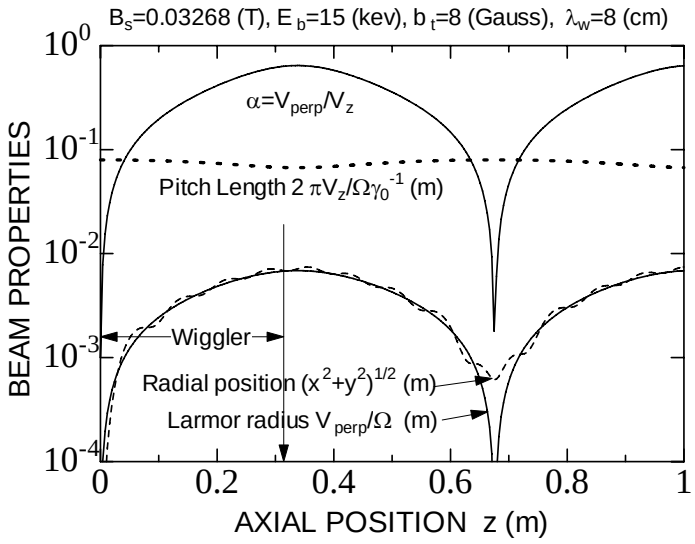

Fig. 17 Designed beam properties.

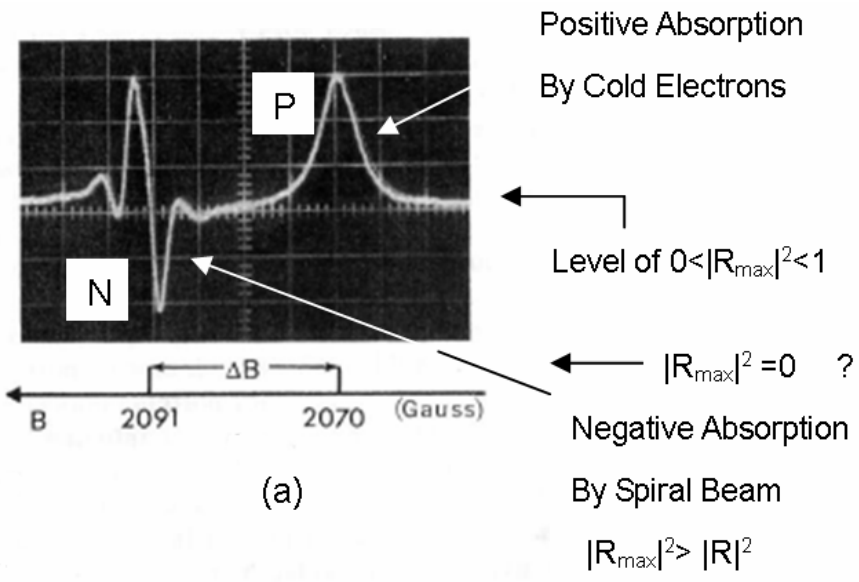

Fig. 18 Physical interpretation of Fig 2(a) in [4].

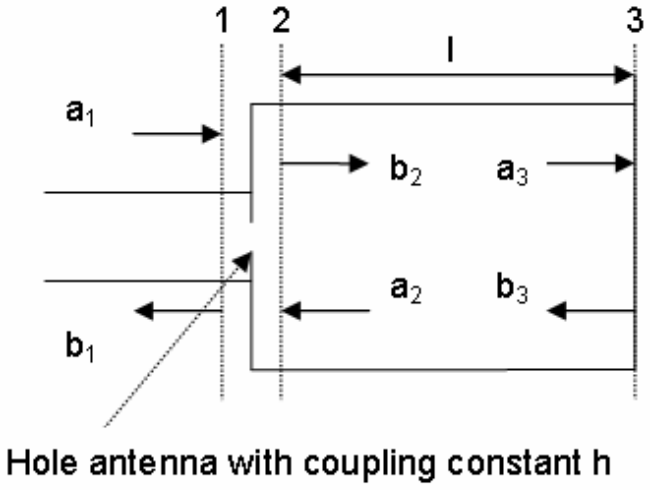

Fig. 19 Model of one-port cavity for analysis.

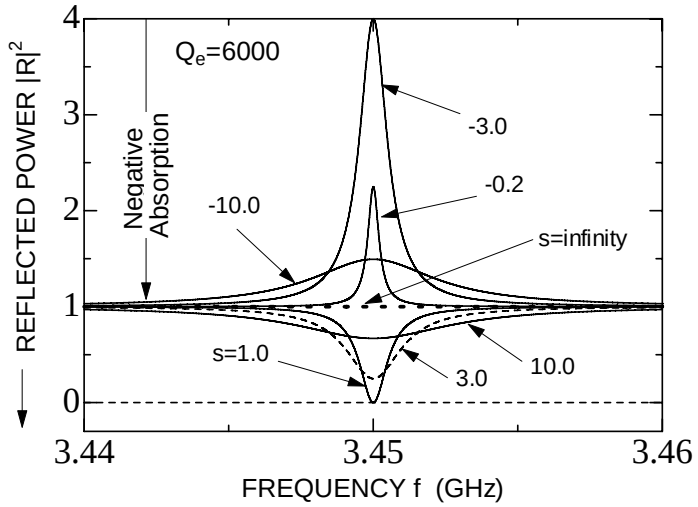

Fig. 20 Calculated reflection coefficient $|R|^2$ vs. frequency from the one-port cavity for various coupling factors $s = Q_u / Q_e$. The portions s>0 and s<0 correspond, respectively, to positive absorption and negative absorption by CRM instability or CIAD.

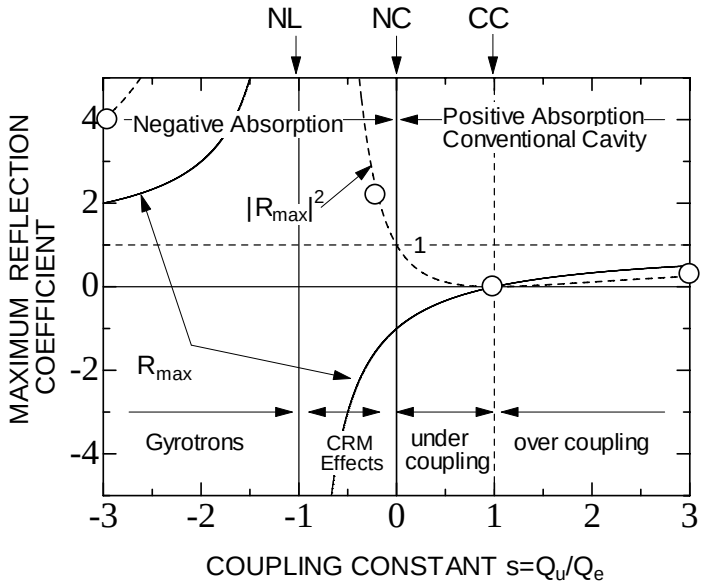

Fig. 21 Calculated maximum reflection coefficient $|R_{\max}|^2$ vs. coupling factor $s = Q_u / Q_e$. The portions s>0 and s<0 correspond, respectively, to positive and negative absorptions. White circles correspond to the curves in Fig. 20.

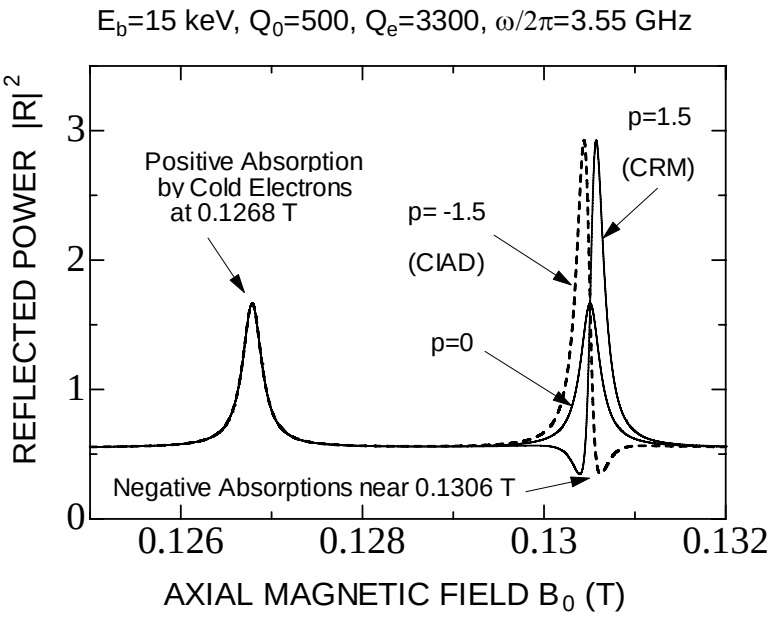

Fig. 22 Calculated curves of absorption expected for CRM (solid curve), p>1.0 in case of $\omega_b^2 \ll \tilde{\Omega}^2$, and for CIAD (dashed curve), p<-1.0 in case of $\omega_b^2 \gg \tilde{\Omega}^2$. Parameters are chosen appropriately to see the schematic properties. Negative absorption is expected for $|p|>1$. Regions of negative absorption are expected to arise, respectively, at low-field side for CRM instability and high-field side for CIAD of $\omega = \tilde{\Omega}$ at $B_0 = 0.1306\,0$ T. The peak at $B_0 = 0.1268$ T is positive absorption by cold plasma.

(a)

(b)

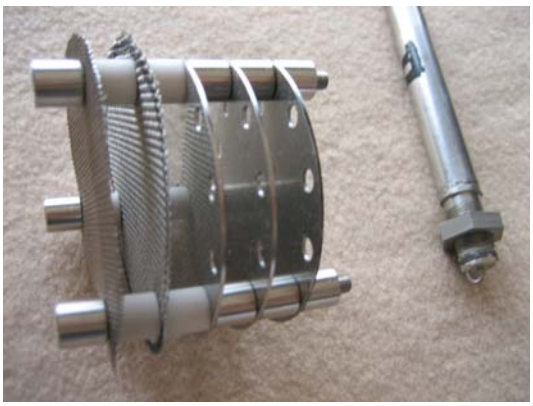

Fig. 23 Fabricated plasma-loaded CRM. (a) Cylindrical TE_{011} cavity with a movable disk inside with two loop antennas. (b) Pair of mesh electrodes to apply dc -15 kV high-voltage (left) and a loop antenna to insert into the cavity in radial direction (right).

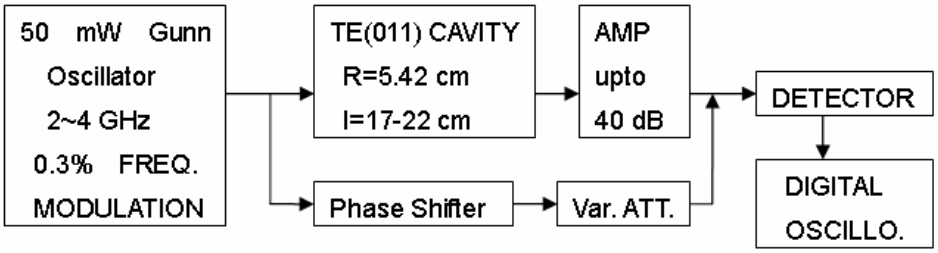

Fig. 24 Constructed microwave interferometer circuits including fabricated TE_{011} mode cylindrical two-port cavity with resonant frequency near 3.45 GHz.

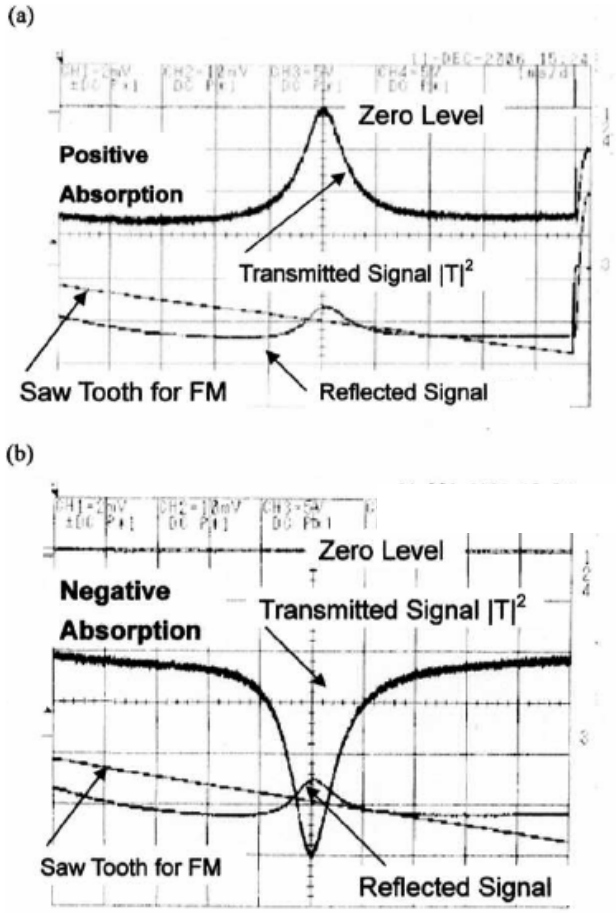

Fig. 25 Transmission signal $|T|^2$ through the empty two-port cavity demonstrating positive and negative absorptions. (a) Positive absorption, when the gain of AMP in Fig. 24 is small, 0 dB. (b) Negative absorption, when the gain of AMP in Fig. 24 is large, 7.5 dB. Simulated negative absorption is observed, because rf power is created in the cavity at resonance 3.454 GHz.

Table 1 Designed parameters

No.	Parts or Apparatus	Designed Value	Estimated Errors	Refer Text
(1)	Mesh Electrodes	SUS304		Fig. 23(b)
	Diameter	70 mm		
	Thickness	0.2 mm		
	Interval	10 mm		
	Beam Energy E_b	15.0 keV	Unknown	Fig. 16
(2)	Pin Hole Aperture	SUS304, 1 mm thickness disk		Fig. 23(b)
	Hole diameter	1 ~ 10 mm	Adjustable	
	Number of disks	3		
(3)	Wiggler Windings	Double Helixes		**3.1**, Figs 1, 10 ~ 17
	Diameter $2a$	36.5 mm		Figs 10 and 11
	Pitch Length λ_w	80 mm	± 2 mm	
	Total Length L	320 mm (4 turns)		

	Current I_{tot}	40 A	Adjustable	Fig. 12
	Magnetic Field b_t	8.0 Gauss on the axis	Adjustable	Eq. (2)
	Conductors	4 mmϕ Copper Wire		
	Axial Magnetic Field B_s	0.03268 T, 72.3 A	3 %	
	Pitch Factor V_θ / V_z	0.65	0.52 ~ 0.83	Fig. 14
(4)	Mirror Field			Fig. 1(c)
	Mirror Ratio	3.88	Adjustable	
	Pitch Factor V_θ / V_z	1.28	Adjustable	
(5)	TE_{011} Cavity	304 SUS, Emery Polished		**3.2.2-3.2.4,** Fig. 23(a)
	Diameter	108.3 mm		
	Axial Length l	170 ~ 210 mm	Adjustable	
	Frequency	3.379 ~ 3.454 GHz	Adjustable	
	Pitch Factor V_θ / V_z	1.28	1.02 ~ 1.64	
	Axial Magnetic Field B_0	0.1268 T, 240 A	3 %	
	Number of Gyration N	16 for l=200 mm	14 ~ 19	
	$N(V_\theta / c)^2$	0.6	0.4 ~ 0.8	
(6)	Coaxial Antennas	304 SUS and Machined Ceramic Insulator		Fig. 23(b)
	Total Length	152 mm		
	Outer Diameter	15 mmϕ		
	Center Conductor	1.6 mmϕ SUS Rod		
	Loop Size	5 ~ 7 mm, Hemi-Circle	Adjustable	
	Coupling Factor s	Unknown	Loop size or rotation of antennas are adjusted	Eq. 11, Fig. 21
(7)	Gunn Oscillator	Shimada Rika Co. 7K905 (D5497)		Fig. 24
	Frequency	2.0 ~ 4.0 GHz	Adjustable	
	Power	0 ~ 50 mW	± 1 %, Adjustable	
	Freq. Modulation	0.3 %	Adjustable	
(8)	Amplifier	ALC microwave Ltd., Model-APA0204		Fig. 24
	Amplification	0 ~ 40 dB	Adjustable	
	Saturation	1.0 W		
(9)	Crystal Detector	HP432B, Negative Polarity		Fig. 24
(10)	Oscilloscope	Tektronix, TDS2024		Fig. 24
	Sensitivity	Max 2.0 mV/cm	Adjustable	Fig. 25
	Data Acquisition	USB port to Excel or png picture files		
(11)	System Controller	Hand Made Source to Drive (7)		
	Saw Tooth for FM	12 V(DC) +10 V(max), 1 kHz		
	Oscillo. Trigger Signal	150 V, 5 μs pulse		